

UNIVERSITY OF SONORA



EXACT AND NATURAL SCIENCES DIVISION
PHYSICS DEPARTMENT
POSTGRADUATE IN NANOTECHNOLOGY

Fluorescent Nanodiamonds based Thermometry

THIS THESIS IS SUBMITTED FOR THE DEGREE OF
MASTER IN NANOTECHNOLOGY

PRESENTS:

L.F. Francisco Alejandro Pedroza Montero

HAVING AS DIRECTOR:

Dr. Martín Rafael Pedroza Montero

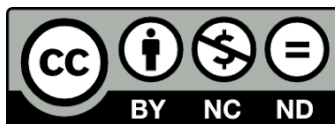
SEPTEMBER 2018

Universidad de Sonora

Repositorio Institucional UNISON



**"El saber de mis hijos
hará mi grandeza"**



Excepto si se señala otra cosa, la licencia del ítem se describe como openAccess

APPROBATORY VOTES

DR. MARIO ENRIQUE ÁLVAREZ RAMOS
Postgraduate Coordinator in Nanotechnology

By means of the present, we are allowed to inform you that the members of the Jury appointed to review the Master Thesis: "**Fluorescent Nanodiamonds based Thermometry**", presented by:

FRANCISCO ALEJANDRO PEDROZA MONTERO

They have reviewed it and each one of the members gives their APPROVAL VOTE since they meet the requirements for obtaining the Master's Degree in Nanotechnology:

Dr. Martín Rafael Pedroza Montero

Dr. Jesús Armando Lucero Acuña

Dr. Raúl Sánchez Zeferino

Dr. Diego Soto Puebla

Dr. Reynaldo Esquivel González (EXTERNAL)

UNIVERSITY OF SONORA

Abstract

Physics Department

Master in Nanotechnology

Fluorescent Nanodiamonds based Thermometry

by Francisco Alejandro PEDROZA MONTERO

Temperature is a property that determines whether a system is in thermal equilibrium with another system. At the nanoscale, issues arise with this very same definition. As we go further into the nanoscale, the thermodynamical equilibrium assumptions may not hold and require a different theoretical approach. Fluorescent nanodiamonds have been proposed in recent works over the past years as temperature sensors and thus acquiring a special category in this context. Nanodiamonds are biocompatible and its optically active color centers (NV Color Centers) allow for optical read-out in a light absorption-emission process. A brief review of the current nanoscale thermometry methods is presented following with an overview of nanodiamonds, from its production to its NV color center main characteristics.

Specifically in this work, commercial nanodiamonds are used and a method to deagglomerate them is proposed. Additionally, for the first time, nanodiamonds in aqueous solution are used to perform fluorescent thermometry and a method to account for fluorescent intensity changes is proposed based on the NV complex light emission.

Contents

Abstract	ii
1 Hypothesis and Objectives	1
1.1 Hypothesis	1
1.2 General Objective	1
1.3 Particular Objectives	1
2 Theoretical Framework	2
2.1 Nanoscale Thermometry and Temperature Measurements	2
2.1.1 Methods	5
Luminescent Methods	6
Non-luminescent Methods	8
2.1.2 Selection of Sensor Type	8
2.2 Nanodiamonds	11
2.2.1 Production of Nanodiamond	12
2.2.2 Nitrogen-Vacancy Color Center	14
Electronic Structure	15
Charge State	17
2.2.3 Creating NV Color Centers in Nanodiamond	18
Implantation	18
Growth	19
Thermal Annealing	19
2.2.4 Size Effects and Stability of Color Centers	20
2.3 Fluorescence Spectroscopy	20
2.3.1 Confocal Fluorescence Microscopy	24
2.3.2 Photodetectors for Fluorescence Microscopy	27
2.3.3 CCD - Charge Coupled Device	27
2.3.4 Types of Noise in a Digital Microscopy Image	28
Dark Current Noise	30
Photon Noise	30
Read Noise	31
2.3.5 Quantum Aspects of Fluorescence	32
Factors Affecting Fluorescence	33
2.3.6 Fluorescent Thermometry Method	34

3	Experimental Setup and Results	39
3.1	Nanodiamonds	39
3.2	Deagglomeration Method	39
3.3	Characterization Techniques	40
3.3.1	Dynamic Light Scattering	40
3.3.2	Transmission Electron Microscopy	42
3.3.3	Confocal Fluorescence Microscopy	45
3.4	Fluorescent Thermometry	47
3.4.1	Tables of Parameters	50
3.4.2	Thermometric Scales	51
	NV ⁰ 's Thermometric Scales	52
	NV ⁻ 's Thermometric Scales	54
4	Conclusions	57

Chapter 1

Hypothesis and Objectives

1.1 Hypothesis

It is possible to establish thermometric scales based upon the fluorescent activity of the nanodiamond's NV color center for potential biological applications.

1.2 General Objective

Make use of nanodiamonds in aqueous solution to measure temperature at the nanoscale based upon the fluorescent activity of its NV color center.

1.3 Particular Objectives

1. Deagglomerate the nanodiamonds by means of Ultra Sonication to the nanometer size.
2. Study the nanodiamonds' characteristic properties by means of the following characterization techniques: Dynamic Light Scattering, Transmission Electron Microscopy and Fluorescence Spectroscopy.
3. Study the nanodiamonds' fluorescent signal at temperatures ranging from 20°C to 60°C with 5°C steps.
4. Fit a curve that accounts for both photon and dark noise with the following parameters: Relative Amplitude (A), Linewidth (Γ), ZPL position (x_0) (photon noise) and background (dark noise).
5. Establish thermometric scales based upon these parameters.

Chapter 2

Theoretical Framework

Physicists often analyze simple problems as they have the higher chance of yielding an analytical solution. Although more general problems lead often to interesting results, these results are intricate or otherwise impossible to solve using simplified analyses. In condensed matter physics, it is often considered infinite lattices that are later transformed by the addition of impurities. Such concepts have been worked by gemologists and material scientists and evolved into how certain defects give rise to desirable properties in materials. Such examples of these impurities are electron-hole donors in semiconductors responsible for tuning the charge carrier densities within a semiconductor chip. Atomic and optical physicists often seek atom-like solid state defects for lasers and masers, quantum information, sensing and other applications. This picture is true to nanodiamonds as they have different color centers and offer surface modification through functionalization. Its optically active color centers can be naturally occurring or synthesized and allow light emission measurements at room temperature. In this work we consider a specific color center, the Nitrogen-Vacancy (NV) color center.

2.1 Nanoscale Thermometry and Temperature Measurements

Temperature measurements at the nanoscale accounts for the determination of temperature and temperature fluctuations at the sub-micron scale [1]. Applications where it is important to be able to measure local temperature at the nanoscale include microelectronics, optics, micro fluid dynamics, chemical reaction and biomedical processes, such as living cells [2-14] and nanomedicine. One example of state of the art temperature measurements is microcircuit temperature mapping among other relevant applications [15-25].

A conventional temperature measurement system typically comprises a transducer to convert a temperature-dependent phenomenon into a signal that is a function of that temperature, a method to transmit the signal from the transducer, some form of signal processing, a display and method of recording the data. A calibration is then used to convert the measured quantity into a value of temperature and the significance of the temperature can then be considered. Temperature measurement systems can be classified according to the physical contact between the transducer and the medium of interest giving invasive, semi-invasive and non-invasive classifications. Examples of each type respectively include thermocouples, thermochromic liquid crystals applied to a surface and observed remotely, and infrared pyrometry [1].

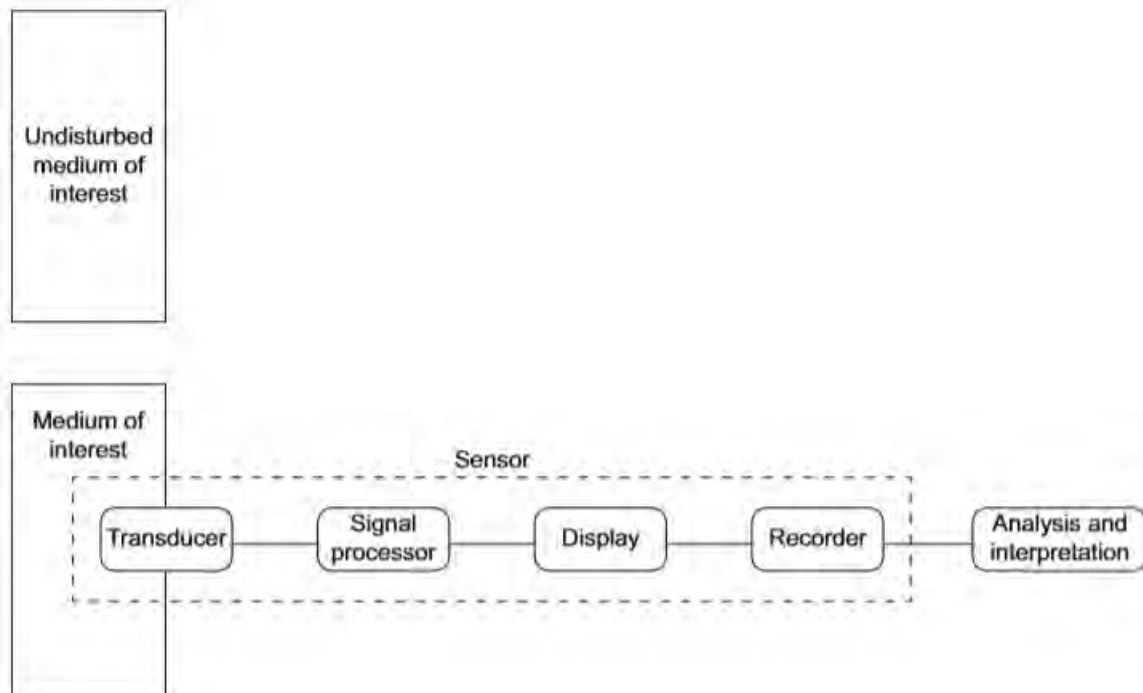


FIGURE 2.1: A comparison between the undisturbed medium and a typical temperature measurement application. Adapted from reference [1].

As technology has advanced over the years, good knowledge of localized heating had to be improved in order to manufacture smaller electronic devices with higher switching speeds and improved reliability. This is of special importance when it comes to local cell temperature, as many biological processes take place and are directly related to that local temperature. For example, a cancer cells exhibit higher temperatures than normal cells due to increased metabolic activity. Cell temperature alters with cellular activity, this can be regarded as cell division, gene expression and enzyme reaction. Temperature measurements at this scale can

provide valuable diagnostic information for biomedical purposes.

Qualitatively speaking, temperature can be regarded as a measure of hotness or coldness of a body. Quantitatively, temperature is derived from the second law of thermodynamics in terms of the rate of change of entropy with energy. This latter definition states that temperature is a property that determines whether a system is thermal equilibrium with another system (or systems). At the nanoscale, issues are derived mainly from the very own temperature definition, as scale goes smaller thermodynamical equilibrium assumptions may not hold [26]. For practical applications, systems are regarded in a non-equilibrium state and it's difficult to determine conditions for at which equilibrium is established at a local system level. A length scale has been proposed to identify whether a canonical energy distribution can be assumed [26]. Taking silicon for example, at very low temperatures (1 K) a length scale of 0.1 m was found providing an indication of the challenge for nanoscale measurements. However, the length scale necessary decreases as temperature rises, up to a limit, after which it's constant. The implications of this nanoscale temperature measurements remain important due to non-canonical energy distributions and non-equilibrium or otherwise ill-defined material properties.

A temperature scale is required for the assignment of numerical values to bodies at different temperatures. The thermodynamic temperature scale is defined by means of perfect heat engines. The unit for the thermodynamic temperature is the Kelvin. As perfect heat engines doesn't exist, the International Temperature Scale of 1990 (ITS-90) has been developed to approximate the thermodynamic temperature. This ITS-90 is constructed by the overlapping of temperature ranges and is believed to represent the thermodynamical temperature to within one standard deviation limit [27]. The ITS-90 enables traceability between the temperature measurement done and the ITS-90 temperature scale.

Most practical temperature measurements are made using devices that have been calibrated against another device which has itself been calibrated according to the ITS-90 guidelines. To calibrate the device means to relate the output value from a measurement system to a known input value. The process is illustrated below. The chain between the thermometer and the ITS-90 is in practice longer and each link increases the uncertainty associated with the measurement [1].

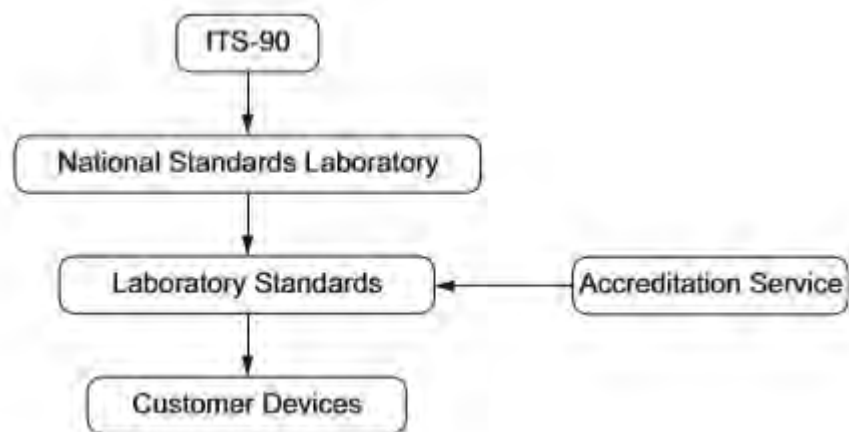


FIGURE 2.2: A typical chain between practical temperature measurement systems and the International Temperature Scale of 1990 [1].

Thermometric systems can be classified according to whether they are characterised by well established equations of state (that relate directly to temperature), known as primary or if they need calibration, then known as secondary.

2.1.1 Methods

Thermometry methods and technologies have been developed over time, simple examples are liquid in glass thermometry, thermocouples and resistance temperature devices, all of which have been adapted to the nanoscale. Remote observation approaches have been investigated; such as Raman, Fluorescence and optical interferometry, to enable temperature measurements within a cellular media, allowing in vivo cellular thermometry. These methods are classified according to Luminiscent Methods and Non-Luminiscent Methods.

1. Liquid and solid-in-tube nanotube thermometry.
2. Resistance.
3. Thermocouples, based on the Seebeck effect.
4. Coulomb blockade.
5. MEMS (microelectromechanical systems) based resonator quality factor or Fermi-level shift.
6. Thermochromic liquid crystals, based on crystal phase transitions.
7. Infrared thermography, based on Planck blackbody emission.

8. Fluorescence.
9. Thermoluminescence or thermographic phosphor thermometry.
10. Thermorefectance, based on the temperature dependence of reflection.
11. Raman, based on inelastic scattering of monochromatic light.
12. Brownian motion.
13. Near-field scanning optical microscopy.
14. Scanning thermal microscopy, using an atomic force microscope with a thermocouple, thermistor or platinum resistance thermometer tip.
15. Transmission electron microscopy.
16. Optical interferometry, based on thermal expansion or refractive index change.

Luminescent Methods

To successfully carry on a thermometry method, the thermal dependence of phosphor luminescent intensity, band shape, peak energy, relative intensities and excited states lifetimes could be used for temperature measurement. A typical thermometry method requires a luminescent probe, applied and bonded to a surface, or incorporated within a medium (water for example), a light source (such as a laser) and a detection system. Many luminescent probes have been synthesized and studied, examples are: organic dyes, quantum dots, polymers and organic/inorganic hybrid matrices incorporating emitting centers [1].

1. **Organic complexes:** These complexes' thermal dependence can be used based on parameters such as the excitation or emission wavelength range required and are of interest because of their solubility and vectorisation. In references [29,30], the authors studied a Ru(phen) and PtTFPP embedded within a crystal structure, which are examples of organic complexes, assessing their maximum temperature sensitivity. Another instance can be found in reference [31], where the authors propose a thermometry method based on a ratio of monomer and excimer intensities.
2. **Quantum dots:** Quantum dots (QDs) are nanocrystals based on a semiconductor material with a range of 2 to 10 nm. These QDs offer a high surface to volume ratio, yielding a quantum mechanical behaviour. Such behaviours are exhibited in properties

such as temperature dependent luminescence, which is used for thermometry. Examples of these type of probes are ZnS coated CdS [32,33]. Factors that are of interest for QD thermometry are bluing, bleaching and blinking under laser excitation [34,35]. Holmes et al. [36] reported that QDs with a covert of an inert material improves their thermometry performance while another authors [37] report desings for QDs in vivo applications.

3. **Phosphors:** Thermographic phosphors exploit the temperature dependence of luminescence, this can be observed by depositing a thin film on top of the system of interest for thermometry. Two common response modes are of use: 1) pulsed and 2) continuous illumination [38,39]. In the first instance, the phosphor exhibits an exponential emission decay whose time constant is temperature dependent. In the seconds instance, the ratio of the emission intensity of two spectral lines are used as they are temperature sensitive. Different kinds of phosphors doped with rare earths have been studied for thermometry, from the use of lanthanide coordination polymers [40], chromium doped aluminum oxides [41] and zinc silicate [42]. These phoshors detailed characteristics have been exploited for fluorescence spectra measurements [43] in order to determine absolute temperature. Authors in reference [44] reported different phosphors for thermal gradient measurements.
4. **Biomolecular Intracellular Thermometers:** These thermometers range from fluorescent probes (such as nanodiamonds) [45], dyes [46], proteins for gene expression control [47], materials for controlled release of chemicals (temperature dependent) [48,49], quantum dots, near IR imaging and the heating of nanoparticles to induce a cell response at a given temperature. Authors in reference [46] exploit the use of a dye (RhB) as temperature indicator within a single cell. The heating of gold nanoparticles injected into a cell (combinated with optical readout of electron spin resonance in single atomic defects in nitrogen vacancy (NV) diamonds as the sensor) has been demonstrated [50].
5. **Optical interferometry:** This technique provides of both local temperature and thermal gradient (such as thermal expansion). Interferometers measure distances in optical paths between two light beams, one of these bypasses the section of interest. A more complicated approach was done by authors in reference [51], where they determine the variation of the refractive index for a microwire.

Non-luminescent Methods

Different technologies have been developed for nanoscale thermometry based on non-luminescent methods. Examples of this are scanning thermal microscopy, carbon nanotube thermometry and biomaterials [1].

1. **Scanning Thermal Microscopy:** This technique comprises of a junction of diameter of 20 to 100 nm, forming a probe tip which is scanned over the surface of interest. Resistance temperature devices can be mounted on top of the probe, to then determine the thermal conductivity of a sample [52-57].
2. **Carbon Nanotube Thermometry:** Modern temperature measurement systems comprise of liquid in glass, originally proposed from authors in reference [58], using gallium as thermometric liquid with the use of a scanning electron microscope in order to observe the meniscus, which is temperature dependent. Examples of thermometric liquids have been demonstrated such as ZnO nanotubes [59], Ga₂O₃ nanotubes [60] and In₂O₃ nanotubes [61]. The use of nanotubes for thermometry provides thermal contact between microscope and the sample of interest and has been explored by authors in reference [62].

2.1.2 Selection of Sensor Type

The selection of a specific sensor (or otherwise system) for thermometry involves the consideration of a number of factors, which are:

1. Uncertainty;
2. Temperature range;
3. Thermal disturbance;
4. Level of contact;
5. Size of the sensor;
6. Transient response;
7. Sensor protection;
8. Availability; and

9. Cost.

Method	Spatial resolution/ μm	Temperature resolution/K	Response time/ μs
Infrared thermography	10	10^{-1}	10
Thermoreflectance	10^{-1}	10^{-2}	10^{-1}
Raman	1	10^{-1}	10^6
Thermocouple	10^2	10^{-1}	10
Fluorescence	10^{-1}	10^{-2}	10
Near-field scanning optical microscopy	10^{-2}	10^{-1}	10
Liquid crystals	10	10^{-1}	10^2
Scanning thermal microscopy	10^{-1}	10^{-1}	10^2
Transmission electron microscopy	10^{-2}	10^{-1}	10
Optical interferometry	1	10^{-5}	10^{-3}

FIGURE 2.3: Typical spatial resolution, temperature resolution and response times for a range of nanoscale-relevant temperature measurement methods, adapted from reference [1].

For nanoscale applications the small scale and specific requirements may dictate a bias for a particular method. Despite the choice, considerations about the uncertainty associated with the measurements are needed. A common assumption is that because fundamental physics is being used, there is no need to consider a measurement uncertainty. However, simplified analysis could be of use to evaluate the thermal changes associated with the probe-medium interaction of interest [63]. This may involve a conduction equation analysis accounting for differences in thermal motion between the undisturbed medium, and that with the probe embedded, or may involve a thermal radiation calculation to evaluate whether the presence of a probe has altered the thermal radiation exchanges significantly [1].

Fluorescent nanodiamonds are an excellent platform as a luminescent probes for thermometry as their optically active NV color center is physically dependant of local nanodiamond temperature; in addition, fluorescent spectroscopy allows for light emission measurements over a range of temperatures with nanometer scale resolution, capturing fluorescent spectra for each temperature scan. These spectra, specifically they zero phonon line emission curves, can be analyzed with a simplified equation with a set of parameters to later describe their thermometry scales.

Method	Principle	Typical resolution			Advantages	Disadvantages
		δx (μm)	δT (K)	δt (μs)		
Infrared thermography	Planck blackbody emission	10	10^{-1}	10	<ul style="list-style-type: none"> Well implemented commercial technique Provides temperature image profile of the surface 	<ul style="list-style-type: none"> Detector saturation at high temperatures Difficulties on the precise estimation of the emissivity of the surface materials Spatial resolution for the temperature detection, which is Rayleigh limited (not all "hot bodies" are perfect blackbodies, in the physical meaning of the term)
Thermoreflectance	Temperature dependence of the reflection	10^{-1}	10^{-2}	10^{-1}	<ul style="list-style-type: none"> High thermal and temporal resolution Quantitative and qualitative measurement 	<ul style="list-style-type: none"> Requires the calibration of the reflectivity index Spatial resolution limited by the diffraction limit Thermoreflectance coefficient is not available for every material and depends on excitation wavelength and thickness of the optical layer
Raman	Inelastic scattering of monochromatic light	1	10^{-1}	10^6	<ul style="list-style-type: none"> No sample preparation needed Works in solids and liquids Small volumes ($<1 \mu\text{m}$ diameter) can be probed Precise temperature calibration 	<ul style="list-style-type: none"> Highly time-consuming technique implying image point analysis as slow as 0.5 point s^{-1}
Micro-thermocouple	Seebeck effect	10^2	10^{-1}	10	<ul style="list-style-type: none"> Spatial resolution (at one dimension) of 25 nm 	<ul style="list-style-type: none"> Low signal and crosstalk with fluorescent molecules The thermometer is separated from the active region of the device limiting, at very short timescales, the access to it Additional fabrication effort required Voltage reflections and capacitive coupling limit the timescale for transient thermometry of the device
Fluorescence thermography	Temperature dependence of quantum efficiency/lifetime/intensity	10^{-1}	10^{-2}	10	<ul style="list-style-type: none"> Diverse experimental techniques to measure temperature High temperature sensitivity Ratiometric algorithms are independent of illumination source 	<ul style="list-style-type: none"> Photobleaching limits the long-term intensity and lifetime determination High-expensive excitation sources and detectors to measure temperature using lifetime-based algorithms
Near-field scanning optical microscopy	Use near field to improve optical resolution	10^{-2}	10^{-1}	10	<ul style="list-style-type: none"> Spatial resolution below the Rayleigh limit (100 nm) 	<ul style="list-style-type: none"> Depends on the surface characteristics Only access to surface temperature Slow temperature acquisition Vacuum and/or cryogenic temperatures required
Liquid crystal thermography	Crystal phase transitions (change colour)	10	10^{-1}	10^2	<ul style="list-style-type: none"> Diverse materials available commercially for different temperature ranges Fully integrated with electronic devices 	<ul style="list-style-type: none"> Yields a semi-quantitative temperature map, unless a detailed calibration is performed A layer of the probe must be placed over the sample Not compatible with liquid systems
Scanning thermal microscopy	AFM with thermocouple or Pt thermistor tip	10^{-1}	10^{-1}	10^2	<ul style="list-style-type: none"> Uses AFM tips to simultaneously measure temperature and determine the surface roughness Sub-micrometric spatial resolution 	<ul style="list-style-type: none"> Slow acquisition times Limited to solid samples Requires fundamental knowledge of tip-sample heat transfer
Transmission electron microscopy	Thermal expansion	10^{-2}	10^{-1}	10^1	<ul style="list-style-type: none"> High spatial resolution 	<ul style="list-style-type: none"> Vacuum required Difficult to transpose for practical applications
Optical interferometry	Thermal expansion or refractive index change	10^0	10^{-5}	10^{-3}	<ul style="list-style-type: none"> Compatible with different CNTs Can be integrated in remote detection systems All optical temperature determination 	<ul style="list-style-type: none"> Temperature determination by image analysis Crosstalk with other stimulus as strain/stress and bending Low spatial resolution in the transverse direction

FIGURE 2.4: Summary of the advantages, disadvantages and general applications of high-resolution electrical, near- and far-field thermal techniques. The typical spatial (δx), temporal (δt) and temperature (δT) resolutions of each method are also included, this table has been adapted from reference [65].

2.2 Nanodiamonds

Diamond nanoparticles were discovered more than fifty years ago, long before nanomaterials became a focus of materials frontiers and just a few years after the first man-made bulk synthetic diamond in 1955 [66,67]. Nanodiamonds (NDs) in nature have existed for billions of years, present within the protoplanetary media of certain types of stars [68] and as part of the composition of meteorites [69]. The first man-made nanodiamonds were produced by detonating carbon containing explosives in an oxygen-deficient environment to avoid carbon oxidation (detonation nanodiamond (DND)) [66]. Since then, numerous methods of nanodiamond synthesis have been discovered, such as laser ablation [70], high-energy ball milling of diamond microcrystals grown at high static pressure and high-temperature (HPHT) [71], chemical vapor deposition (CVD) [72], microplasma-assisted ND formation from ethanol vapor at atmospheric pressure [73], chlorination of carbides [74], ion irradiation of graphite [75], electron irradiation of carbon onions [76] and ultrasound cavitation [77]. However, detonation synthesis remains a primary source of nanodiamond particles at a production level of tons per year.

Among nanomaterials, diamond nanoparticles occupy a special place due to their combination of outstanding mechanical performance, chemical resistance, versatile surface chemistry, biocompatibility, and unique optical and electronic properties originating from dopants (such as Nitrogen). They have emerged as a key platform for many nanoscience and nanotechnology developments [78]. Nanodiamond's super-hardness and exceptional chemical resistance promote use in novel wear-resistant polymer and metal coatings [79]. In addition, the abrasive nature of diamond lends itself to applications in lubricant additives, providing extremely smooth sliding surfaces and a dramatic decrease in friction [80]. The high refractive index, scattering efficiency, and biocompatibility of NDs make them appealing for use in healthcare products such as sunscreens [81]. Especially impressive are demonstrations of ND applications in the biomedical arena. Crystallographic defects in the diamond lattice give nanodiamond photoluminescent properties useful as fluorescent biolabels or biomarkers in the life-science community [82,83] or for anti-counterfeiting or authentication purposes [84]. Such color centers include nitrogen-vacancy (NV) and silicon-vacancy (SiV) complexes. The spin properties of selected color centers, particularly the nitrogen-vacancy center, can be optically detected, stimulating developments of high-resolution magnetometers, atomic-size sensors for electric fields, and quantum measurement of the temperature gradient within living cells [85,86]. Nanodiamond-mediated drug delivery has also been widely explored, and their versatility as carriers for a broad array of compounds ranging from small molecules to proteins and

nucleic acids has been demonstrated [87]. The unique set of properties attractive for drug delivery applications includes exceptional biocompatibility, large carrying capacity, and a wide array of surface functional groups. The latter can be used for ligation with anti-bodies for targeted drug delivery as well electrostatic drug binding and environment-dependent sustainable release [87,88]. One example of particular importance is the integration of nanodiamond with doxorubicin demonstrating marked improvements in tumor treatment efficacy at much lower dosing [89], while recent progress in nanodiamond-mediated drug delivery in orthopedic, dental, and ophthalmic sectors emphasize the broad applicability of nanodiamonds as a carrier for therapeutics [87]. The combination of nanodiamonds biocompatibility, affinity to therapeutics, and stable fluorescence make them an attractive nanoplatform for theranostic applications.

The combination of the nanodiamonds' properties and its plausible surface functionalization through biomolecules such as drugs or genes would allow a single *nano* platform for detection and treatment and as well as labelling or a multi purpose nano sensor. In the same sense, scientific studies show that nanodiamonds have a water layer [91,92], conveying a possible mechanism for rehydration for cell's membrane. Recent studies indicate that carboxylated nanodiamonds act as reducing agents, promoting less oxidative damage in biological systems [93]. Nanodiamonds are carbon nanostructures that have attracted the scientific community due to its potential in biomedical applications.

2.2.1 Production of Nanodiamond

Diamond is known to be one of the hardest materials as their crystal lattice bonds correspond to high binding energies (~ 285.1 eV) of sp^3 electron bonds (carbon-carbon) forming the diamond lattice [94]. Moreover, diamond has a center cubic lattice structure, is transparent and has a very high thermal conductivity (~ 2000 $Wm^{-1}K^{-1}$) [95]. Diamond is classified according to the number of impurities present in the diamond lattice, as these impurities often translate to different physical properties. As Nitrogen is the most frequent impurity in diamond, its relative amount is used to determine the type of diamond.

Beside natural deposits, synthetic diamond is an alternative for its production. The two main techniques nowadays (from nm to mm, respectively) are high pressure high temperature (HPHT) and chemical vapor deposition (CVD). Another instance for diamond production is

Type	Impurities	Origin
Ia	$\approx 0.1\%$ nitrogen, nitrogen cluster	98% of all natural diamonds
Ib	$\approx 0.05\%$ nitrogen, nitrogen cluster	$< 0.1\%$ in nature, includes high-pressure synthesis
IIa	few ppm nitrogen	rare in nature
IIb	less nitrogen than IIa, other elements present such as Boron, Magnesium and Silicon.	extremely rare in nature, produced by high-pressure synthesis

TABLE 2.1: Table enlisting types of diamond and its classification according to present impurities.

by shock wave assisted growth [94].

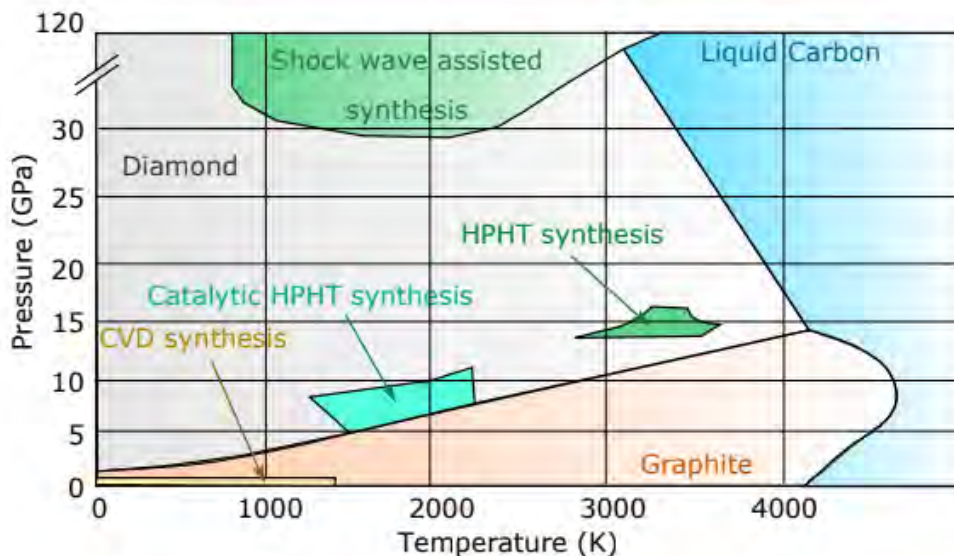


FIGURE 2.5: Phase diagram of Carbon. [96]

High-Pressure High-Temperature: This synthesis tries to mimic the natural diamond forming conditions (deep within the earth mantle) using a hydraulic press to transform from a graphitic phase of carbon to the diamond phase [97-98]. This type of diamond synthesis corresponds to type I with >50 ppm concentration of nitrogen. Higher and lower nitrogen concentrations have been explored, from thousands to tens of ppm [99]. Additionally, high quality diamonds of type IIa and IIb are created by suppressing the incorporation of nitrogen and using a getter like titanium, aluminum, boron, copper and/or germanium [97]. Diamond synthesized by HPHT are in several sizes, from millimeter down to several nanometers [100].

Chemical Vapor Deposition: This synthesis grows diamond directly onto a substrate by deposition of carbon atoms from a methane diluted vapor. The substrate is to be placen in

an evacuated chamber and a mixture of methane/hydrogen is injected. A chemical reaction takes place (i.e., $\text{H} \cdot + \text{CH}_4 \rightarrow \text{H}_2 + \text{CH}_3 \cdot$) where the aromatic hydrogen transforms methane into radicals. If close to the substrate, these chemicals react with the surface creating a solid thin film. To create more of these reactions, the substrate is heated. Plasma is usually created above the substrate surface (plasma enhanced CVD) or even hot wires are used (hot filament CVD). However most efficient growth of diamond is established by streaming the precursor through a plasma arc leading to more aromatic hydrogen promoting diamond deposition [101].

Shock-wave assisted synthesis: This synthesis is similar to HPHT as the regime reproduced is similar during the shock wave synthesis. Explosives are used to create conditions needed in a very short and intense way. This synthesis comprises of a chamber filled with a carbon-containing precursor (graphite, for example) mixed with explosives [102]. After the detonation, the atomic carbon condenses to a liquid phase and later transforms to solid diamond resulting in nanometer sized (tens of nanometers) diamond crystals and detonation soot [103]. Explosives often used are TNT (trinitrotoluol) and RDX (hexogen) and mixtures the nitrogen content to several ppm [104-105]. Purifications allows to concentrate the final product up to 99.95% [106]. Most recent shock wave synthesis reported by [107] demonstrates a 1.4 nm diamond with very little spread in size.

2.2.2 Nitrogen-Vacancy Color Center

The Nitrogen Vacancy Center (NV) is a point defect in the diamond lattice consisting of a single carbon substitution by nitrogen with a vacancy next to it [108]. Besides the fact that NV is a color center that can be excited and detected in the visible range, the unique electronic level structure of the negatively charged defect allows initialization and readout of the spin-sublevels just by optical means [109]. As the electron spin state of the NV is also coupled to its local environment, sensing applications for various physical quantities have been demonstrated [110-118]. Also the use as a qubit for quantum computing and various schemata for quantum processing have been shown [119]. Almost all mentioned applications are based on utilizing the ground state of NV [94].

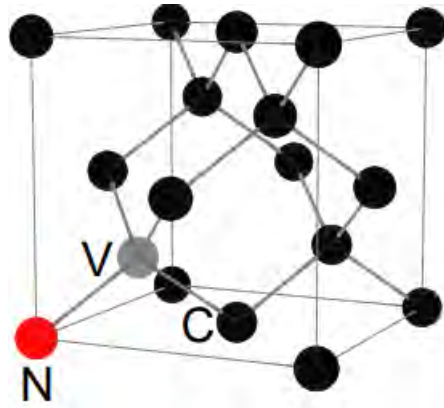


FIGURE 2.6: An NV center embedded in the diamond crystal lattice. The diamond lattice constant is 0.3567 nm, and the carbon-carbon separation is 0.1545 nm [164].

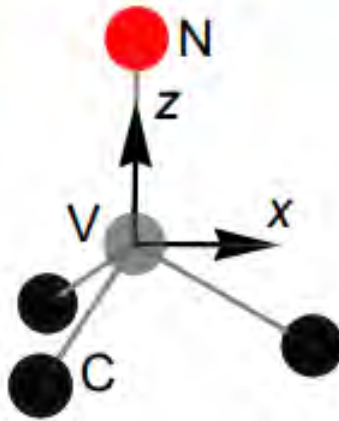


FIGURE 2.7: An NV center complex with the x -, z - axes labeled.

Electronic Structure

As the NV complex is formed by a nitrogen next to a vacancy, this nitrogen has three neighbor carbon and two unbound electrons contributing to the defect. In addition, there are three carbon orbitals next to the vacancy, containing one electron each. Assuming that both nitrogen and carbon orbitals are in a sp^3 configuration it is found by applying linear combination of orbitals that this NV complex corresponds to a C_{3v} point group for the individual electron within the complex [120]. The molecular orbitals are $a_1(1)$ and $a_1(2)$ (A_1) and two degenerated orbital state e_x and e_y [121]. As this description corresponds to a total of 5 electrons inside the NV complex, this is known as the NV^0 charge state. To form the NV^- an additional electron has to be captured. This electron donor is suspected to come from a substitutional nitrogen in the vicinity. The electronic configuration for the six electrons in the lowest state $a_2^2 a_1^2 e^2$, it is found possible spin configurations [121]: 2 singlet states (1E and

1A_1) and 1 triplet state (3A_2). In the excited state configuration $a_1^2a_1^1e^3$, a singlet $^1E'$ and a triplet 3E is found. As the triplet states are lower in energy, because they have the lowest amount of unpaired electrons (Hund's rule), they form the ground (GS) and first excited state (ES) of the NV^- [121]. ES and GS are split by the energy of ≈ 1.945 eV. If the NV relaxes back to the GS it can either do that directly by emitting a red photon (corresponding to a ≈ 1.945 eV) or decay via spin-orbit coupling to a meta-stable state (MS) system by emitting an infrared photon with 1.190 eV [122]. This last infrared transition originated from a singlet-singlet transition in the electronic lowest state that are assumed to form the metastable (MS) system. Treating both singlet states as one level, the NV can be described by a three level system. Most interesting, the coupling rates (k_{ij} transition coefficients) of NV are spin depended and as a consequence the adjusted spin state can be read out optically [94]. After excitation of the NV from the GS (with the spin quantum number $m_s = \pm 1$), the probability for an inter-system crossing from the ES to MS is higher than in the case of $m_s = 0$. This latter spin configuration is preferred as it is most stable, leading to a reduction of possible round trips during excitation in a given time and therefore a drop in fluorescence as the transitions MS to GS is spin forbidden and takes additional time. This is explained as spin polarization into the GS with spin state $m_s = 0$ [123].

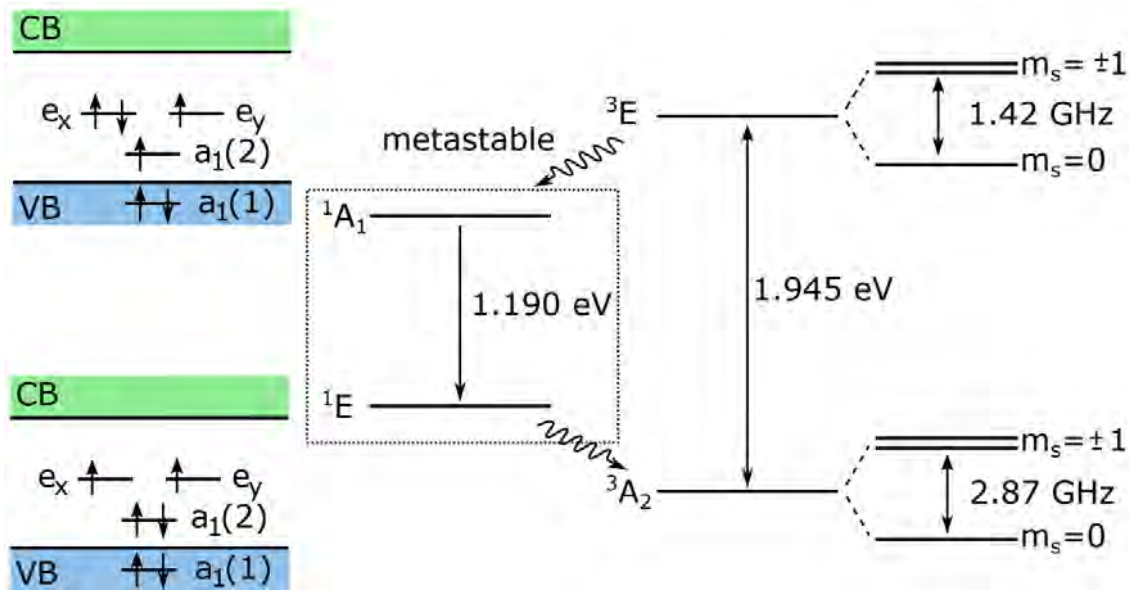


FIGURE 2.8: Electronic structure of the Nitrogen Vacancy center in diamond. *Left:* State population of electronic levels forming the NV^- . *Right:* State picture describing level transitions at room temperature. Adapted from reference [94].

Charge State

There are 3 known charge states of the NV complex, two of them (NV^0 and NV^-) exhibit fluorescent properties in the visible range. For the neutral nitrogen vacancy center (NV^0) it has been proposed that in principle optical read out and spin polarization like for the NV [124] should be possible, up to now no one could make practical use of NV^0 spin system only [94]. Moreover, a positively charged nitrogen vacancy center (NV^+) exists. Several publications give hint to its existence [125,126], but no fluorescence has been detected up to now [127]. Therefore the NV complex is first converted to NV^- , a certain nuclear spin state is to be adjusted to then discharge the NV complex to the NV^+ state.

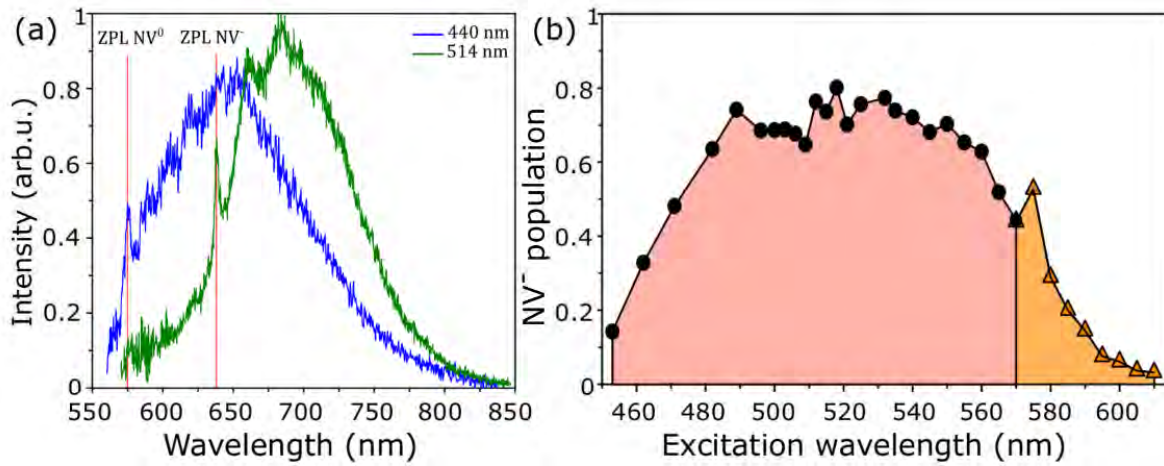


FIGURE 2.9: Dependence of the NV charge state for different laser excitation wavelengths. (a): The fluorescence spectra of NV^- (green) and NV^0 (blue) detected from the same NV center for different excitation wavelengths. (b): Probability to be in NV^- charge state. Adapted from reference [94].

Excitation wavelength allows to switch to NV^0 or vice versa in a probabilistic way, this arises from a ionization and recombination process of the NV^- state, if the energy of the photons is high enough a linear dependence of the ionization from laser excitation power can be found [128]. After photon excitation, a second photon absorbed promotes an electron from the saturated electronic states to the conduction band. If an additional electron from the conduction band is captured by the unfilled $a_1(2)$ state in an Auger process the NV complex will end up in the NV^0 ground state [129]. Similar considerations are of use in the process of NV^0 to NV^- conversion.

It has been found in the process of recombination of NV^0 to NV^- that the neutral charge state plays an important role, because excitation at the ZPL of NV^0 leads to an enhancement probability to be in NV^- state. After absorbing a photon, an electron is promoted from the

$a_1(2)$ to an electronic level in the NV^0 state. After capturing an additional electron by photon absorption, the NV complex is in the NV^- charge state. As also other impurities or charge traps can take over the role as an electron donor, the conversion from NV^0 to NV^- can still work for excitation wavelengths below the ZPL of NV^0 [129].

2.2.3 Creating NV Color Centers in Nanodiamond

Color defects in diamond arise from factors such as growth procedure, concentration and type of impurities, all of which give rise to the color and type of a given diamond. These colors are described as color defects within the diamond lattice and their position relative to each other is also relevant. As thermometry goes, these color defects are preferred as close to the surface to achieve contact with the medium of interest, enhancing the thermal interaction. The relative position is important as it directly determines the quantum behaviour of spin interaction, to within certain radius, of coupled color defects.

Several methods have been proposed to create or otherwise promote the NV color center creation, among the most relevant methods: ion-implantation [139-149], growth [150-152] and thermal annealing [153-155].

Implantation

The most established technique giving desired results is ion-implantation, as it allows to specifically create NV or SiV with more or less deterministic density in high vacuum. Therefore one typically accelerates Nitrogen, Silicon or molecules with a given energy towards the diamond. After penetrating the diamond surface the ion interact with the diamond lattice leading to crystal defects like vacancies. After annealing the diamond at several hundred degrees °C the vacancy starts to diffuse. If they reach the vicinity of nitrogen or silicon they can form an NV center (or any other complex, depending on the defects). To enhance lateral resolution the diamond is often masked where no defects are desired. For example photo-resist [139,140], mica [141] and even the tip of an atomic force microscope (AFM) [142] has been used reaching implantation resolution of several tens of nanometer and below. As lateral extension of implantation can be controlled quite good, axial resolution is depending on implantation energy and if implanting into a crystal on the crystal orientation towards the implantation beam. As crystal have a well defined ordered lattice arrangement they provide long straight channels through the crystal. If an ion enters such a channel it can penetrate

much deeper into the crystal before it collide with lattice atoms. As a consequence the axial ion distribution after implantation is stretched [144]. To suppress the so called channeling effect typically mono-crystalline substrate is tilted by an angle of 7° [145]. To provide high axial positions typically low energies implantation around several keV are used. But with decreasing implantation energy also the yield of creating NV drops drastically even below 1% for below 10 keV, as the ratio of created vacancies per nitrogen atom decreases [142]. If a specific density of NV is desired, one can increase the implantation dose [146], or co-implant with other ions like carbon or molecules [147,148]. With increasing ion dose also the probability of creating other spin defects that alter the coherent properties increases. One of the most prominent representatives is the so called di-vacancy, which is a pair of vacancy defects within the crystal lattice. By adding a p-doped layer on top of the diamond, vacancies become positively charged and the probability to form di-vacancies decreases as the two positively charged vacancies repulse each other [149]. In addition the NV formation yield increases.

Growth

Besides implantation NV can also be created by the addition of nitrogen gas during CVD. This allows lateral positioning in a thin layer via δ -doping [150] or even preferential alignment of NVs inside a bulk sample [151]. By intentionally introducing Silicon atoms also SiV can be created. SiV are also a common side impurity during diamond synthesis, originating from glass windows in the growth reactor. As ND are often produced via HPHT synthesis, nitrogen is already present in the diamond grain. To enhance the concentration of optical active defect within a single grain typically high energy (MeV) proton, helium or electron irradiation is used to produce additional vacancies [152].

Thermal Annealing

To heal out the diamond crystal it has to be heated at least about 600°C [153]. At such temperature the vacancy defect start to diffuse and leave the crystal via the surface. Typically annealing temperatures are $T > 800^\circ\text{C}$. Also the temperature used to anneal diamond material after implantation plays an important role for the quality of produced defect: Best annealing parameters for nanodiamond are 800°C to 900°C for 1h to 2h in terms of brightness [152,154]. For diamond bulk material Naydenov et al. [155] showed that post annealing at around 1200°C for 12h leads to an increase of NV spin coherence times. They explain

this behavior by the mobility of other spin defect also leaving the diamond crystal at higher temperature.

2.2.4 Size Effects and Stability of Color Centers

As diamond material reduces in size the surface to volume ratio increases drastically. As an interesting consequence thermodynamical calculations suggest that the preferred phase of carbon materials is size dependent. Whereas for diamond particles bigger than 5.2nm the graphite-phase is most stable, for particles from sizes ranging from 1.9nm to 5.2nm diamond is more preferable [156]. In Addition, also the capability to host impurities like nitrogen or silicon decrease with size and are dependent on the surface termination, as it defines the crystallographic morphology of the whole particle. In case of NV the stability in diamond is even less preferred at this sizes [157], resulting in more substitutions in bigger sizes. In contrast, comparable calculations for the color center SiV in the very same set of diamonds result in a high stability of this defect for hydrogenated diamonds of sizes down to 1.1 nm, and there is also sufficient experimental proof for the existence of such small fluorescent nanodiamond (fNDs) [158-160]. The smallest diamond hosting NV found so far is around 5 nm [161].

Quantum confinement: With reduce size of ND the particle transforms from bulk-like to quantum behavior starting at a size of 4.5 nm [162]. As a consequence also the optical band gap in diamond increases [162,163] that can also influence the electronic transitions. In case of SiV this leads to shift of the ZPL towards the blue. Time-dependent density functional theory (TD-DFT) calculations estimated a shift of 0.03 eV for 1.8 nm and 0.12 eV for 1.1 nm sized NDs [158].

Nanodiamonds and their NV color centers responsible for their light emission properties in the visible range make of them a great platform for thermometry measurements, this mainly by the use of fluorescent spectroscopy.

2.3 Fluorescence Spectroscopy

This type of spectroscopy analyzes fluorescence from a given sample. By the use of a beam of light (laser source most commonly), the sample is illuminated and emits light. This emitted light corresponds to a difference in the vibrational energy level of the referred sample.

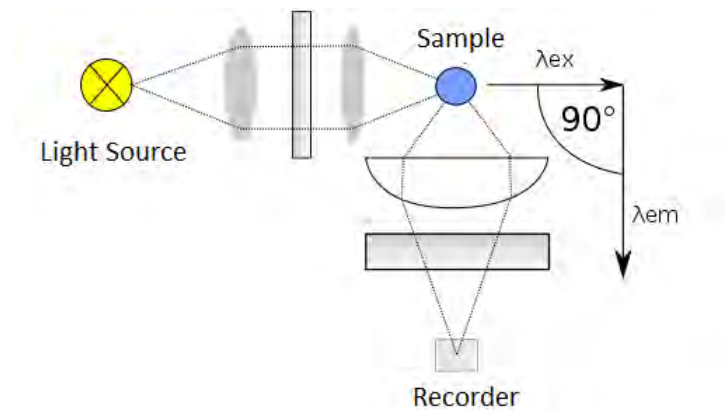


FIGURE 2.10: A simple design of a fluorescent spectrometer set up.

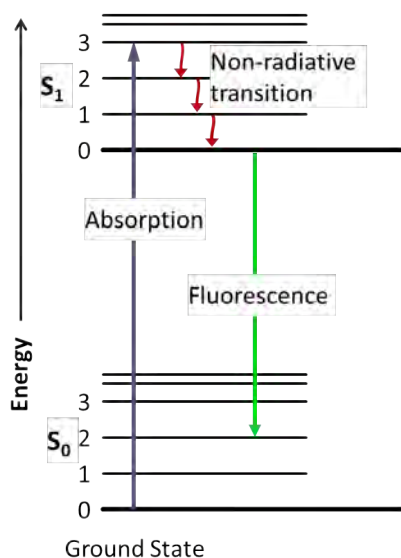


FIGURE 2.11: A simple Jablonski diagram illustrating how an electron behaves in a fluorescent process.

After energy absorption, the electron jumps from its ground state to an electronically excited level and very rapidly decays to a lower excited level, losing some energy in non-radiative transitions to finally relax to its ground state emitting a photon equal in energy to the energy difference between levels.

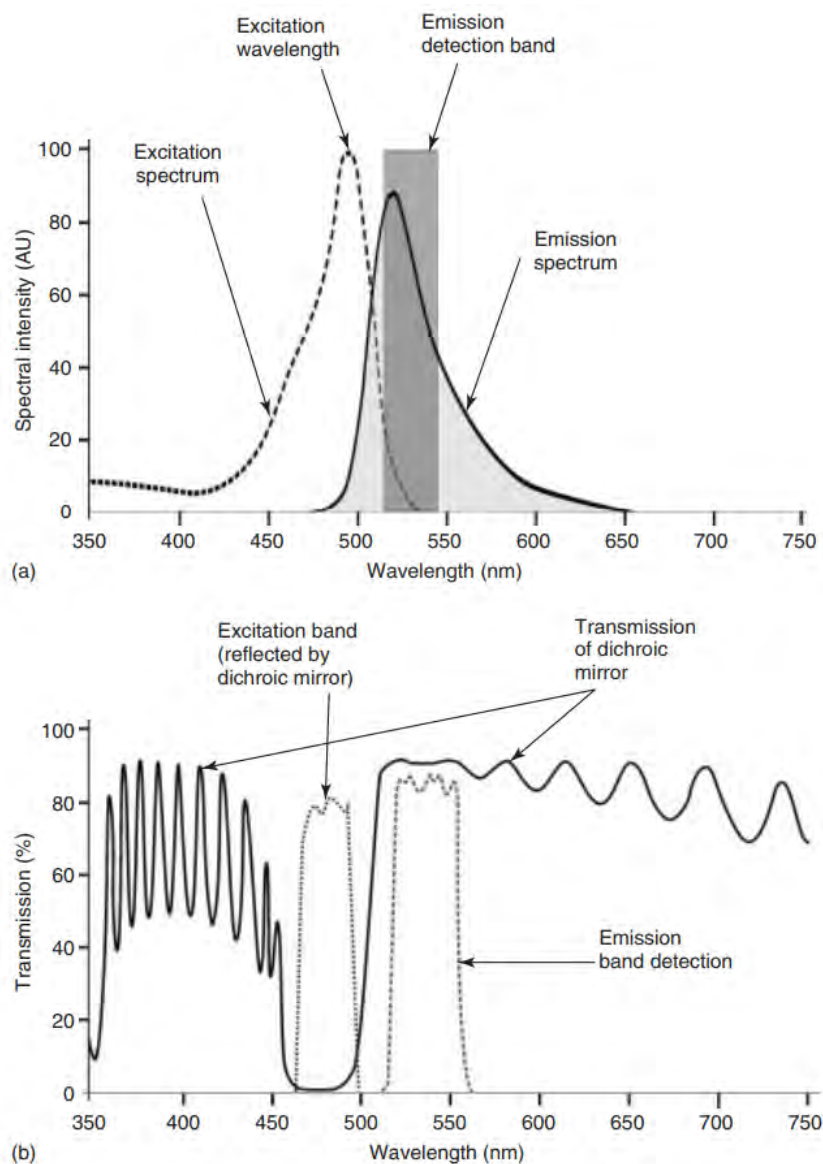


FIGURE 2.12: Spectral properties of a typical fluorescent label, fluorescein (a), and the characteristics of a filter set suitable for selecting the excitation band and detecting fluorescence emission (b).

Fluorescence is excited by light that is emitted by a mercury lamp or a laser source onto a given sample. The exciting light is reflected toward the sample by a dichroic (two-color) mirror. This special mirror is positioned at 45° angle toward the incoming light and reflects photons of a selected wavelength but allows light of longer wavelengths to pass through, filtering the incident wavelength. The dichroic mirror is selected for a given application, that is, it is made to reflect the chosen exciting wavelength and allow the passage of the expected fluorescence. It is important to realize that the efficiency of converting exciting light into fluorescence is usually low, that is, only one out of many exciting photons is converted into

a photon of a longer wavelength and subsequently detected as fluorescence. Moreover, the fluorescence is emitted by the sample in all directions, but only a selected light cone, that is, a fraction of this fluorescence, is collected by the objective lens. Consequently, fluorescence is weak in comparison with the exciting light and has to be efficiently separated and detected.

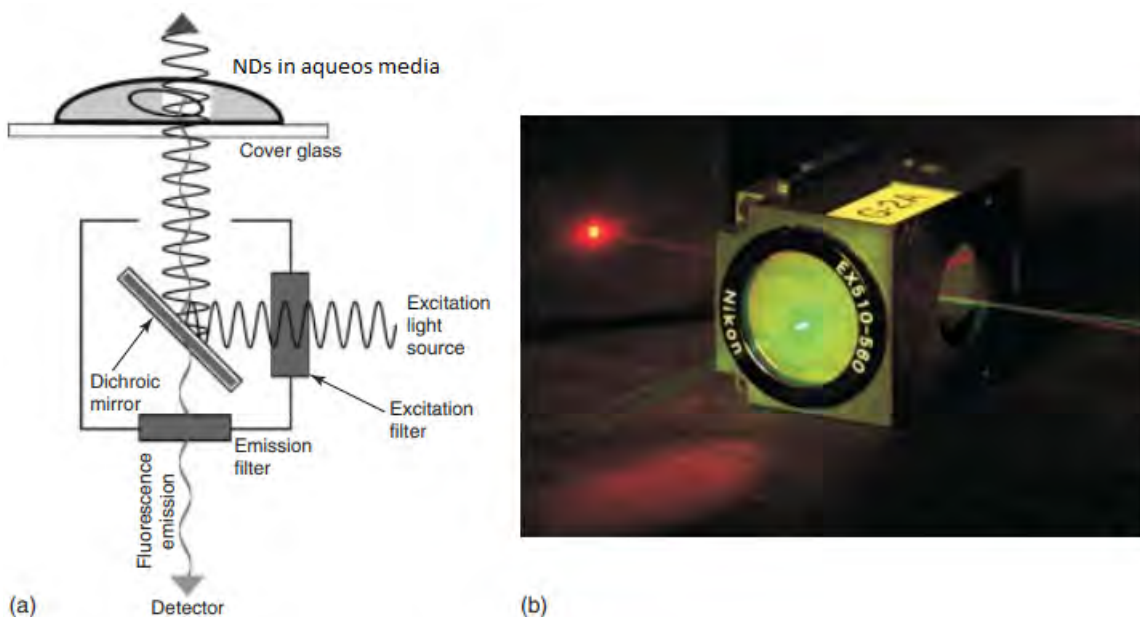


FIGURE 2.13: A fluorescence microscope filter block. (a) A schematic diagram of a typical filter block containing an excitation filter, a dichroic mirror, and an emission filter. The exciting light emitted by a light source is reflected by the dichroic mirror toward the specimen; the fluorescence emission has a longer wavelength than the exciting light and is transmitted by a dichroic mirror toward the ocular or a light detector. (b) A photograph of a microscope filter block, which reflects green but transmits red light.

In the original fluorescence microscope design, removing the excitation filter from the light path allowed the intense exciting light into the eyepiece and the eyes of the observer. Even in the case where the objective lens does not allow UV light to pass through, this would be very dangerous. In the epifluorescence design, there is no danger of sending the exciting light directly into the eyes of the observer. Even when the dichroic and excitation filters are removed, the exciting light will not be incident directly onto the ocular. This does not mean, however, that it is safe to look through the microscope with the exciting light source turned on, and all the filter blocks removed out of the light path. When filters are removed, the exciting light is still sufficiently reflected and scattered to pose a hazard to the eyes of the observer.

2.3.1 Confocal Fluorescence Microscopy

Confocal fluorescence microscopy is a technique that provides true three dimensional optical resolution. This resolution is achieved by designing an instrument so that it is primarily sensitive to a specimen's response coming from an in focus plane, or by removing the contributions of out of focus planes. The three dimensional resolution is accomplished by actively suppressing any signal coming out of out of focus planes. This is achieved by using a pinhole in front of the detector as the figure below depicts.

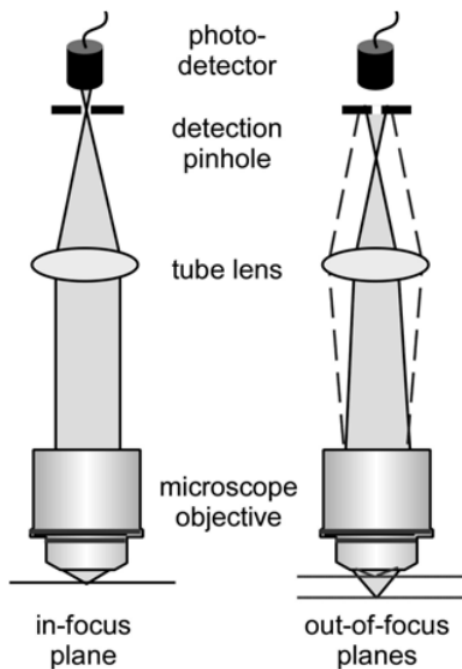


FIGURE 2.14: Principle of Confocal fluorescence microscopy. Light coming from out of focus planes is largely blocked by the pinhole mechanism.

In a confocal fluorescence microscope, the specimen is generally illuminated by a laser. The term *excitation* rather than *illumination* will be used in what follows, since it more explicitly refers to the contrast-generating process: the excitation of fluorophores, through absorption, causing detectable fluorescence. The light coming from the laser passes through the pinhole, is reflected by a dichroic mirror, and focused by a microscope objective to a small spot in the specimen. The dichroic mirror reflects light of a shorter wavelength (e.g., 488 nm Argon laser) while transmitting that of longer wavelength (e.g., the fluorescence greater than 510 nm from a particular specimen). Specific dichroic mirrors can be manufactured for relevant wavelength regions for excitation and fluorescence.

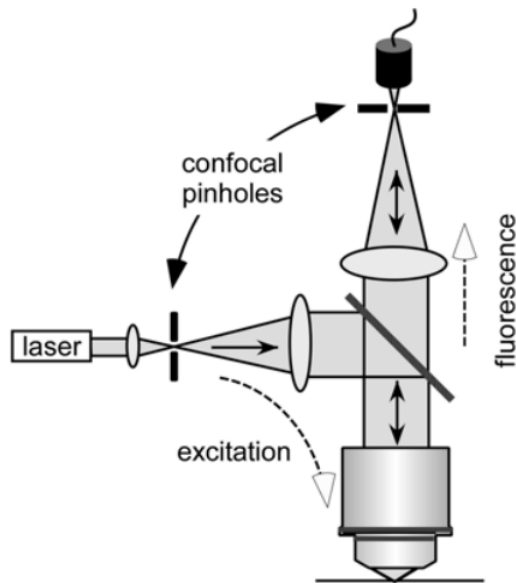


FIGURE 2.15: Excitation of the specimen in confocal fluorescence microscopy by a laser. A fraction of the fluorescence emitted by the fluorophores in the specimen is collected by the microscope objective and imaged onto the detection pinhole in front of a photo-detector.

The human eye requires contrast to perceive details of objects. Several ingenious methods of improving the contrast of microscopy images have been designed, and each of them opened new applications of optical microscopy in biology. The simplest and very effective contrasting method is dark field. It exploits the scattering of light on small particles that differ from their environment in refractive index, the phenomenon known in physics as the Tyndall effect. A fixed and largely featureless preparation of tissue may reveal a lot of its structure if stained with a proper dye – a substance that recognizes specifically some tissue or cellular structure and absorbs light of a selected wavelength. This absorption results in a perception of color. The pioneers of histochemical staining of biological samples were Camillo Golgi (an Italian physician) and Santiago Ramon y Cajal (a Spanish pathologist). They received the 1906 Nobel Prize for Physiology or Medicine. A revolutionary step in the development of optical microscopy was the introduction of phase contrast proposed by the Dutch scientist Frits Zernike. This was such an important discovery that Zernike was awarded the 1953 Nobel Prize in Physics. The ability to observe fine subcellular details in an unstained specimen opened new avenues of research in biology. Light that passes through a specimen may change polarization characteristics. This is a phenomenon exploited in polarization microscopy, a technique that has also found numerous applications in material science. The next important step in creating contrast in optical microscopy came with an invention of differential interference contrast by Jerzy Georges Nomarski. In his technique, the light incident on the sample

is split into two closely spaced beams of polarized light, where the planes of polarization are perpendicular to each other. Interference of the two beams after they have passed through the specimen results in excellent contrast, which creates an illusion of three-dimensionality of the object.

However, by far the most popular contrasting technique now is fluorescence. It requires the use of so-called fluorochromes or fluorophores, which absorb light in a specific wavelength range, and re-emit it with lower energy, that is, shifted to a longer wavelength. Today, a very large number of different dyes with absorption from the UV to the near-infrared region are available, and more fluorophores with new properties are still being developed. The principal advantages of this approach are a very high contrast, sensitivity, specificity, and selectivity. The first dyes used in fluorescence microscopy were not made specifically for research, but were taken from a collection of stains used for coloring fabrics. The use of fluorescently stained antibodies and the introduction of a variety of fluorescent heterocyclic probes synthesized for specific biological applications brought about an unprecedented growth in biological applications of fluorescence microscopy. Introduction of fluorescent proteins sparked a new revolution in microscopy, contributed to the development of a large amount of new microscopy techniques, and enabled the recent enormous growth of optical microscopy and new developments in cell biology. A Japanese scientist, Osamu Shimomura, and two American scientists, Martin Chalfie and Robert Y. Tsien, were awarded a Nobel Prize for Chemistry in 2008 for the discovery and development of green fluorescent protein (GFP) in biological research.

Lasers emit light of discrete wavelengths, characterized by high stability both spatially (the direction in which the beam is propagated is fixed; so-called beampointing stability), and temporally – both on a short and long timescale. The stability of the light beams and the ability to focus them to a diffraction-limited spot was an important advantage of lasers over mercury arc lamps. The disadvantage, however, was their high cost combined with a limited number of usable emission lines for exciting popular fluorophores. For instance, the popular 25 mW argon ion laser provided the 488 and 514 nm lines, which were not optimal for working with the most popular (at that time) pair of fluorescent dyes – fluorescein and rhodamine. Other gas lasers that are often used in confocal fluorescence microscopy include krypton–argon (488, 568, and 647 nm) and helium–cadmium (442 nm). Solid-state lasers, including a frequency doubled neodymium-doped yttrium aluminum garnet (Nd:YAG, 532 nm), are also used.

Currently, the price of standard gas lasers has decreased, and a wide selection of various single line lasers and lasers emitting a broad wavelength spectrum are available. Durable diode lasers became available as well. Moreover, new low-cost sources of light, LEDs, have become available. LEDs are semiconductors, which exploit the phenomenon of electroluminescence. Originally used only as red laser pointers, they now include a range of devices emitting in ultraviolet, visible, or near-infrared spectral region. The critical part of an LED is the junction between two different semiconducting materials. One of them is dominated by negative charge (n-type) and the other by positive charge (p-type). When voltage is applied across the junction, a flow of negative and positive charges is induced. The charges combine in the junction region. This process leads to a release of photons. The energy (wavelength) of these photons depends on the types of semiconducting materials used in the LED. A set of properly selected LEDs can now be used as a source of stable exciting light in a fluorescence microscope. LEDs are extremely durable, stable, and are not damaged by being switched on and off quickly. These advantages will probably make them very popular not only in scanning confocal microscopes but in standard fluorescence microscopes as well.

2.3.2 Photodetectors for Fluorescence Microscopy

Currently, fluorescence microscopes are equipped with suitable systems for light detection, image digitization, and recording. The most common light detector in a standard widefield fluorescence microscope is a charge-coupled device (CCD) camera, while photomultipliers are used in laser scanning confocal microscopes. Other types of light detectors, including intensified charge-coupled device (ICCD) and electron multiplied charge-coupled device (EMCCD) cameras, as well as avalanche photodiodes (APDs), are gaining increasing importance in modern fluorescence microscopy.

2.3.3 CCD - Charge Coupled Device

In a camera based on a CCD, an image is projected onto an array of semiconducting light-sensitive elements that generate an electric charge proportional to the intensity of the incident light. Two types of sensor architectures are currently produced: front-illuminated charge-coupled device cameras, where light is incident on an electrode before reaching the photosensitive silicon layer, and back-illuminated charge-coupled device cameras, where the incoming light falls directly on the silicon layer. Note that the structure of an FI CCD is

similar to the anatomy of the human eye. In the retina, it is the nerve wiring that faces the incoming light. Only after light has passed the layer of nerve cells that are not sensitive to light, can the photons interact with rhodopsin in the photoreceptors.

When the array of light-sensitive elements (capacitors, photodiodes; in digital microscopy called picture elements or pixels for brevity) of a camera is exposed to light, each of them accumulates an electric charge (Figure 2.17). These charges are later read one by one. An electronic control system shifts each charge to a neighboring element and the process is repeated until all charges are shifted to an amplifier. When the individual charges are dumped onto a charge amplifier, they are converted into corresponding voltage values. This process is repeated until all the light detected by a microscope in all pixels of the field of view is eventually translated, point by point, into voltage values. The values of these voltages are subsequently converted into discrete values (digitized) and translated into the levels of brightness (intensity of light) on the display screen. A CCD camera's sensitivity and its ability to record strong signals depend on a number of factors, including the level of electronic noise and the ability to accumulate a large number of charges. Weak signals may be undetectable if they are comparable with the noise level. Strong signals may also be difficult to record faithfully. Exposing a CCD array to a large dose of light may result in filling the well with charges and reaching a maximum well capacity (saturation charge). This may cause charges spilling into the neighboring wells and result in deterioration of image quality.

In an ideal situation, only the photons that strike the silicone surface of a light-sensitive element of the camera should actually cause accumulation of an electric charge, which is later shifted and read out. However, some electrons may occur and are recorded even in the absence of any incident light. This contributes to the noise of the displayed image. As fluorescence intensities encountered in microscopy are usually low, the fluorescence signal may be difficult to detect in the presence of substantial camera noise (Read Noise).

2.3.4 Types of Noise in a Digital Microscopy Image

If a light detector were ideal, an image collected in the absence of any specimen should be completely black. However, even in the absence of any fluorescence in the sample, CCD sensors still generate certain readout values that are greater than zero. In laboratory vocabulary, these weak unwanted signals that do not represent fluorescence are generally called *background* or *noise*.

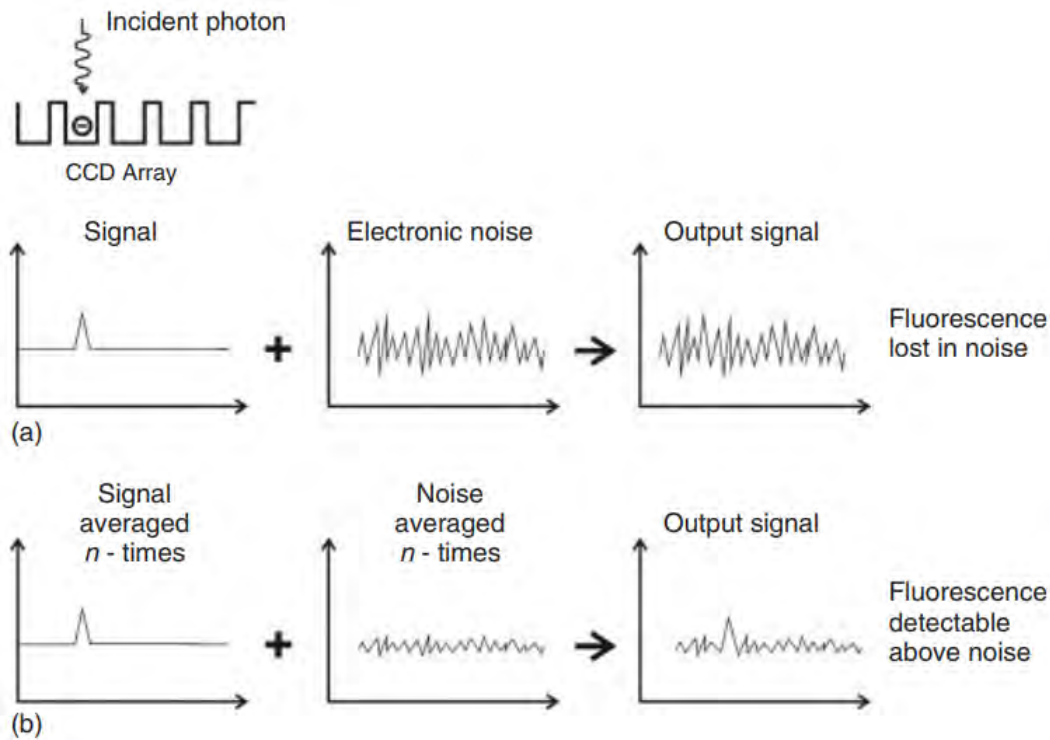


FIGURE 2.16: Signal averaging and detection of weak fluorescence signals. (a) A weak signal cannot be detected if it is comparable with the level of noise generated by the electronics of a camera. (b) When images of stable fluorescence signals are averaged, the noise is averaged out and becomes relatively low in comparison with the signal.

The adverse influence of noise on the quality of the recorded image is understandable. Let us assume that the noise signals have a value in the range between 1 and 10 on a scale of 1–100. If a signal representing fluorescence has an intensity of 80, it will be readily detected, but if a weak signal has an intensity of 10, it will not be distinguishable from the noise. Averaging a large number of image frames should make the signal detectable over the noise level, but an experimenter rarely has the luxury of collecting many images of the same field of view because photobleaching will inevitably diminish the fluorescence signal (this isn't the case for nanodiamonds), while the noise level will remain the same. The range of intensities of fluorescence signals that can eventually be recorded above the level of noise is called the dynamic range of the detector. More precisely, dynamic range is the ratio between the maximum and the minimum level of signal that can be detected. Thus, the dynamic range of a CCD camera is equal to the saturation charge (full well capacity) divided by the readout noise (i.e., the noise generated in the absence of light), when both are expressed as the number of electrons. A higher dynamic range of a camera means a broader range of fluorescence intensities that can be faithfully recorded.

Some sources of noise were mentioned when speaking about the principles behind and construction of various camera types. Generally, one can identify three major sources of noise in a digital microscopy image registered by a camera:

- Dark current noise,
- photon noise and
- read noise.

Dark Current Noise

The dark current (dark noise) arises from electrons that are generated in a well of a semiconductor sensor in the absence of any external light due to electron emission by thermal motion. When the integration time on the CCD chip is increased, the accumulating thermal charge also increases. This leads to a detectable background in the image. As the electron emission is dependent on temperature, cooling the camera chip efficiently reduces the dark current. The dark current can be decreased from the final image by subtraction. Dark current noise should not be confused with background signal arising from low-level autofluorescence or fluorescence arising from nonspecific binding of an antibody in an immunofluorescence preparation.

Photon Noise

The photon noise or shot noise results from the quantum nature of light. It is a term that refers to the temporal distribution of photons arriving at the surface of a sensor. Even if the fluorescence-emitting object is flat and uniformly stained, the frequency of photons arriving at the light-sensitive element of the sensor is governed by chance. The frequency of photon arrival follows the so-called *Poisson statistics*. This implies that the number of photons originating in a given small volume of a continuously illuminated specimen and subsequently reaching the detector varies in different time intervals (we ignore photobleaching for simplicity). This also implies that when the same (nonbleaching) voxel in the specimen is imaged repeatedly, and in a given measurement the number of detected photons is n , the subsequent determinations of the number of photons vary within a range of \sqrt{n} . Shot noise can be quite misleading. Inexperienced microscopists often take the grainy structure of an area in the image for a real variation of the fluorescence signal, or interpret differences between local signal

intensities as evidence for a difference in the concentration of a fluorescence label. However, such features of the image may merely be a consequence of a very low number of photons that are typically collected in fluorescence microscopy studies.

Read Noise

The read noise arises in the process of converting a charge generated in the sensor well into voltage and digitization. Camera manufacturers provide information about the noise generated on-chip by specifying a root-mean-square number of electrons per pixel (RMS per pixel). For instance, $10 e^-$ RMS means that a read noise level of 10 electrons per pixel is expected. Thus, the signal obtained after readout of the charges would show a standard deviation of 10 electrons, even if all pixels contained identical numbers of electrons. At low signal levels, photon noise is the most significant noise contribution. As vendors may interface the same type of a light-sensitive chip with different electronics, the levels of electronic noise in cameras from different sources may also be different.

In addition to these major sources of noise mentioned above, other factors may result in unpredictable signal variability or nonzero levels. These factors include the nonuniformity of photoresponse, that is, noise values dependent on the location in the image sensor, and the nonuniformity of dark current. Nonuniformity of photoresponse is a consequence of the fact that individual pixels in a CCD chip do not convert photons to electrons with identical efficiency. Pixel-to-pixel variation is usually low in scientific grade cameras and generally does not exceed 2%. The correction for differences between light sensitivity of individual pixels can be achieved by recording an image of an ideally uniform fluorescent object, for instance, a dye solution, and creating a correction mask using standard image processing tools. Dark current nonuniformity results from the fact that each pixel generates a dark current at a slightly different rate. The dark current may also drift over a longer period, for instance, owing to a change in the sensor's temperature.

These *noise* concepts are worked in this thesis in the sense to account for Dark Noise (background) and Photon Noise (light emission from the sample) inside a set of parameters that describe the experimental data.

2.3.5 Quantum Aspects of Fluorescence

Fluorescence is a light emission process based on a light absorption process. Excited species are later relaxed to the ground state, releasing this energy in the form of photons. The lifetime of these photons is short, there are two main relaxing mechanisms: non-radiative transitions and radiative transitions (fluorescence). Non-radiative transitions can happen as vibrational relaxation or internal conversion.

Vibrational relaxation happens when energy is transferred as collisions within the sample, this is seen as an increase in local sample temperature. This is an efficient process in which average lifetimes are in the order of $\approx 10^{15}$ seconds. Non-radiative relaxation between two vibrational energy levels (lowest excited state and highest electronic state) can happen as well, known as internal conversion.

Fluorescence in the sample happens when any of the electronic excited states can relax to the ground state. It is similar to absorption as this energy lines are close together and are hard to resolve. The most probable transition is the one with the lowest excited lifetime. This means that fluorescence happens very quickly with respect to those processes without light emission.

It is observed that the fluorescence bands are formed by bands that have longer wavelengths and lower energies than the energy band responsible for their excitation, this is known as Stokes shift. In those cases in which the absorbed radiation is emitted without change in wavelength (same energy) is known as radiation from resonance or fluorescent resonance. Because the energy differences between the vibrational states is approximately the same, both for the ground state and for the excited, the absorption and the emission or fluorescence spectrum of a compound frequently appears as a mirror image from one to another with an overlap that occurs in the resonance line [165].

The following list of concepts has been re-arranged from references [165] and [166], illustrating the most common factors that affect the fluorescent signal and why it is important. The most common factors affecting a material's fluorescent signal are the material's quantum yield, structure, temperature, pH, quenching, concentration and instrumentation.

Factors Affecting Fluorescence

1. **Quantum Yield:** This is a relation between the number of fluorescent molecules versus the number of excited molecules. Highly fluorescent molecules approximate this yield nearly to 1 (meaning every excited molecule fluoresces) and non-fluorescent molecules are have a practically 0 quantum yield.
2. **Structure:** Empirically it is found that fluorescence is particularly favored in molecules that have rigid structures.
3. **Temperature:** The quantum efficiency of fluorescence decreases in many molecules with the increase in temperature, since the increase in the frequency of collisions at elevated temperature increases the probability for the process in which electronically excited states pass to a lower electronic state (often the ground state) by colliding with other molecules. In this process the electronic energy is eventually converted into heat. Since this process involves collisions, the rate at which it occurs depends on how frequently collisions occur. As a result, this process occurs much faster in liquids than in gases. It is sometimes called collision quenching.
4. **pH Effect:** Relatively small changes in pH will sometimes radically affect the intensity and spectral characteristics of fluorescence. Most phenols are fluorescent in neutral or acidic media, but the presence of a base leads to the formation of nonfluorescent phenate ions; for example, serotonin, show a shift in fluorescence emission maximum from 330 nm at neutral pH to 550 nm in strong acid without any change in the absorption spectrum.
5. **Quenching:** Decrease of fluorescence intensity by interaction of the excited state of the fluorophore with its surroundings is known as quenching and is relatively rare. Quenching corresponds to a non-random process. Each example (each different fluorescent probe) is indicative of a specific chemical interaction, so each sample has its own quenching due to its local physical environment].
6. **Concentration:** If the concentration of the fluorophore increases, energy deviations occur and a non-linear behaviour is observed in the emission spectra vs concentration.

7. **Instrumentation:** Different fluorescent spectroscopy experimental setups could be of use and it directly relates to the result obtained, meaning that different experimental arrays relate to different results.

2.3.6 Fluorescent Thermometry Method

Nanodiamond's fluorescent spectrum is that of particular interest as it comes to fluorescence thermometry. Given the local temperature of the fluorescent probe (a nanodiamond with NV centers) we detect a specific fluorescent signal. That is to say we can account for spectra over a range of temperature in order to observe the behaviour of the fluorescent signal of the nanodiamonds and its NV complex. The following figure shows a nanodiamond's fluorescent spectra at room temperature (RT) of 25° , locating the NV emission lines (575 and 638 nm) which are of interest to measure local temperature.

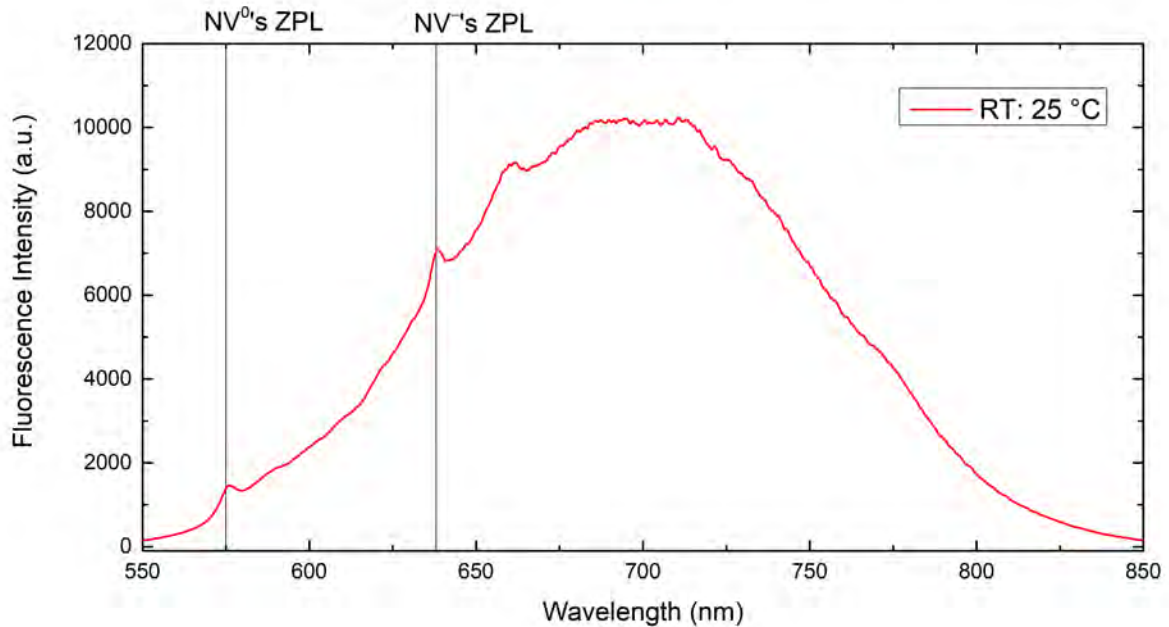
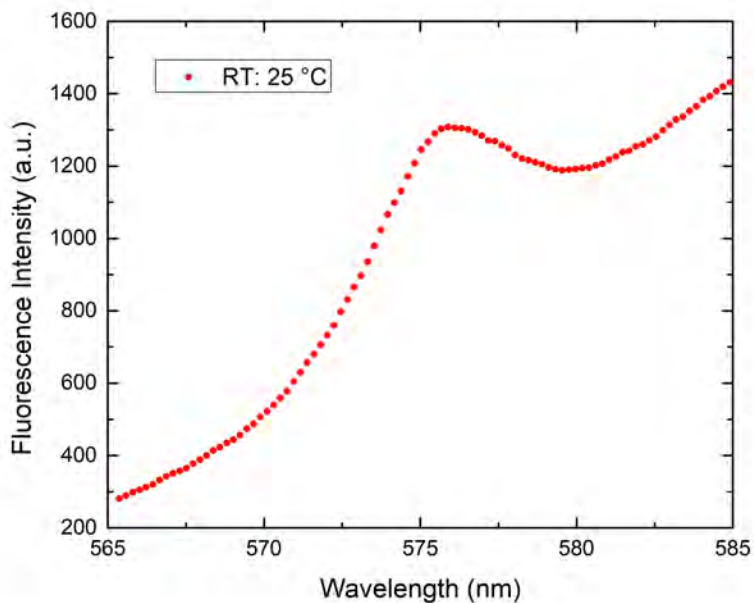
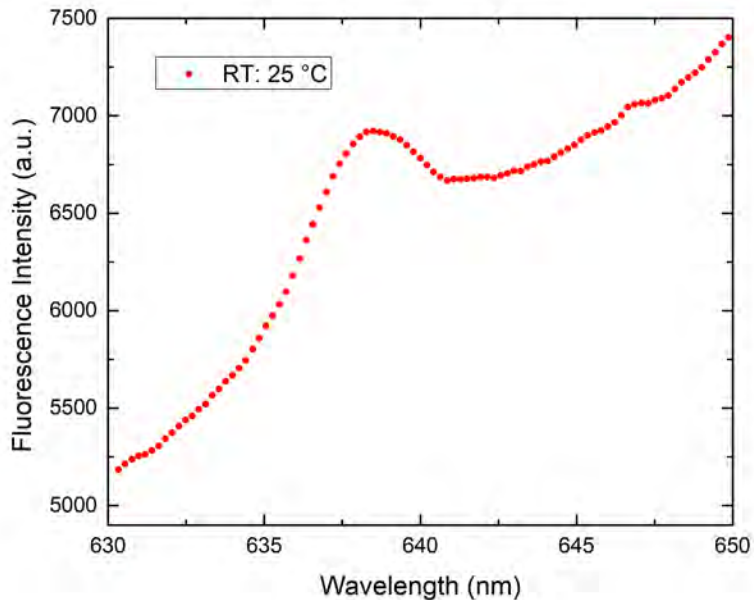


FIGURE 2.17: Fluorescent spectra of nanodiamond's at room temperature (RT) with a 488 nm Argon laser excitation source. The 575 nm label corresponds to NV^0 's zero phonon line and the 638 nm label to that of NV^- 's zero phonon line.

FIGURE 2.18: NV^0 charge state ZPL at RT.FIGURE 2.19: NV^- charge state ZPL at RT.

In the two latter figures, similar spectral features are seen easily. These points data are to be fitted accordingly to account for the background dark noise signal and that coming from the NV's charge state emission. This method, similar to that of Plathotnik et al. [168],

consists of a curve fit of the kind:

$$N = B_0 e^{B_1(x-x_0)} + \frac{A\Gamma^2}{\Gamma^2 + (x - x_0)^2} \quad (2.1)$$

This equation accounts of an exponential background (B_0 and B_1) and a Poisson noise (A , Γ and x_0) contribution. Each ZPL that corresponds to each different charge state (NV^0 and NV^-) of the NV complex are similar in spectral features. These features can be compiled in a list of spectral parameters known as:

1. A : Relative amplitude [a.u.] of a given ZPL's emission,
2. Γ : Linewidth [nm] (or $\frac{1}{2}$ of FWHM) of the ZPL,
3. x_0 : ZPL position [1/nm],
4. B_0 : Pre-exponential factor [a.u.],
5. B_1 : Exponential factor [1/nm],

which correspond to those parameters in equation 2.1 and it's used to minimize equation 2.2. With these parameters for each temperature run, we can build a table of parameters versus temperature in order to establish thermometric scales.

The data analysis is that of a minimizing chi-squared function, which can be carried out as follows:

$$\chi^2 = \sum_n \left(N_n - B_0 e^{B_1(x-x_0)} + \frac{A\Gamma^2}{\Gamma^2 + (x - x_0)^2} \right) \quad (2.2)$$

where N_n corresponds to the number of photons detected in the n th spectral bin (one pixel of the CCD). This idea is illustrated below for any x_0 of choice (either charge state of the NV complex).

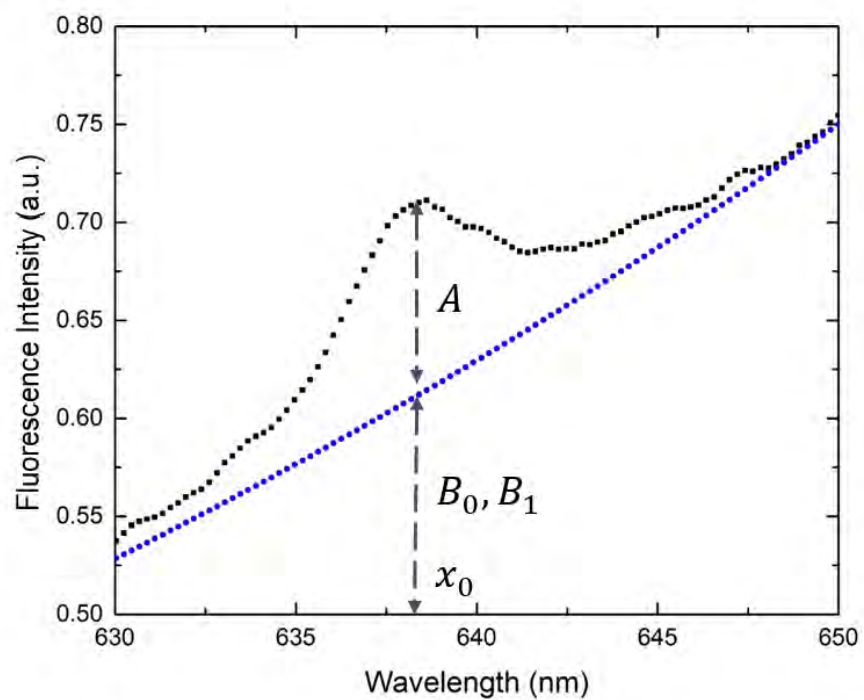


FIGURE 2.20: Blue curve illustrates background noise.

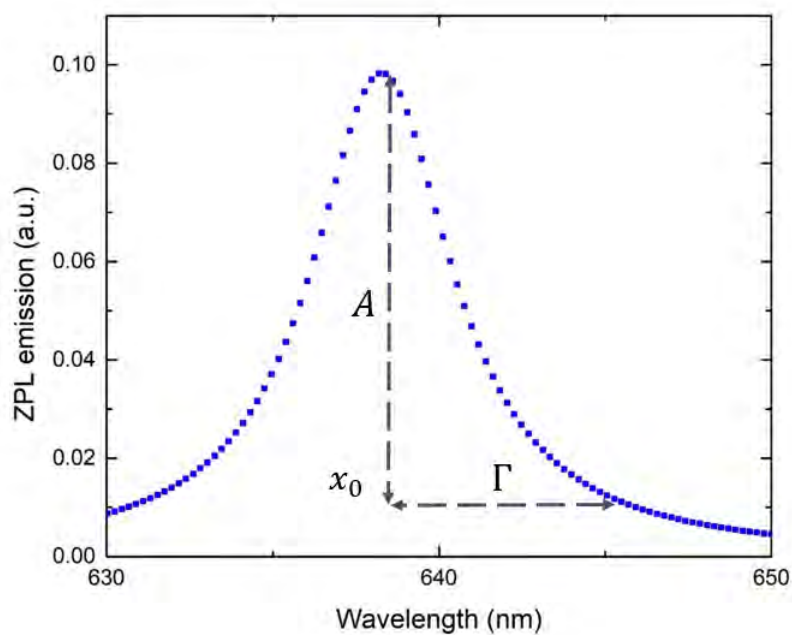


FIGURE 2.21: Curve illustrating Poisson noise and its parameters.

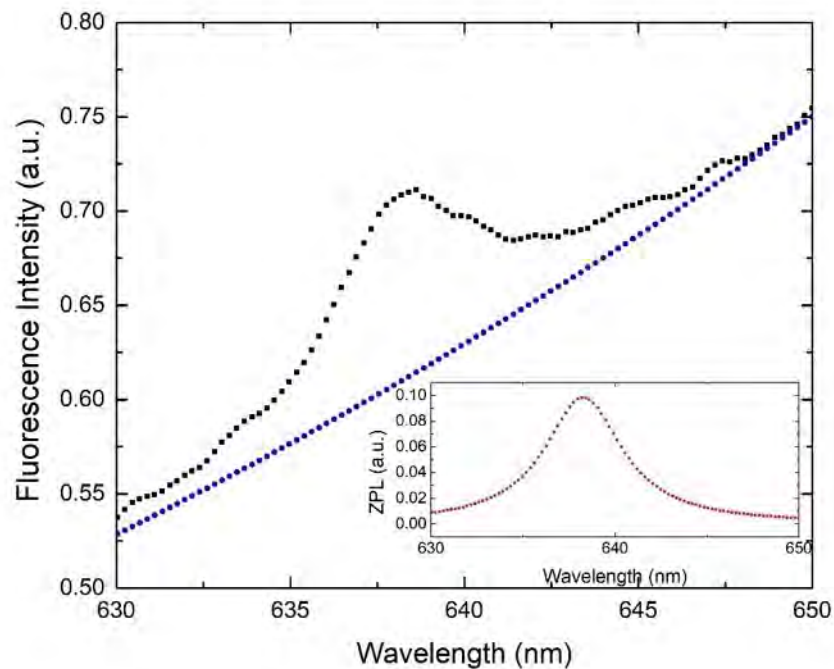


FIGURE 2.22: Blue curve corresponds to background noise and red curve to ZPL emission only, the sum of these two curves are expected to fit the data shown in black.

This method is to be carried on with every spectra at each temperature and thus analyzing the parameters obtained, it can be identified which parameters fit best a thermometric scale.

Chapter 3

Experimental Setup and Results

All data were analyzed and made using OriginPro 9.0 software. Micrographs images from TEM were analyzed using ImageJ editor.

3.1 Nanodiamonds

Fluorescent nanodiamonds (fNDs) obtained from Sigma Aldrich (part no. 798134-5ML) with >800 NV centers/particle at 1% concentration, with a 100 nm average particle size in deionized water. Briefly, nanodiamonds were resuspended in a plastic falcon tube with 1 mL of nanodiamonds in solution mixed with 9 mL of miliQ water (1:10 ratio), resulting in a sample of 10 mL in volume and a concentration of 0.1%.

These nanodiamonds come "as is" in aqueous media and are aggregated up to few microns in size and are not suitable for temperature measurements at the nano scale thus a deagglomeration method is proposed as follows.

3.2 Deagglomeration Method

To deagglomerate the nanodiamonds, a method similar to that of Pedroso-Santana et al. [167] is proposed. Instead of using Silica Beads to assist the deagglomeration process as these authors proposed, nanodiamonds are sonicated without Silica Beads or any other particle. This method eliminates the cleaning process needed for silica particles.

Samples were sonicated with a QSonica Q500 sonicator equipped with a horn-type sonotrode, resting inside a tray with ice packs to prevent heating. The settings used were 60% amplitude, with 5 cycles ON/OFF of 30 seconds in the machine settings.

3.3 Characterization Techniques

3.3.1 Dynamic Light Scattering

Dynamic light scattering measures Brownian motion (random movement) and relates this to the size of the particles. This is based upon that larger particles exhibit a slower motion while smaller particles exhibit a faster one. Zeta potential was analyzed as well by using a special cuvette for electric field application.

DLS and Zeta potential measurements were performed on a Zetasizer Nano ZS series from Malvern Instruments at 25°C with a 30 seconds equilibrium time between each measure. The sample of nanodiamonds were deposited inside a disposable cuvette of 40 μL (ZEN0040) that fits the apparatus. Each sample of nanodiamonds was resuspended in miliQ water in a 1:10 ratio in order to achieve 1:100 ratio inside each cuvette. Nanodiamond's refractive index (2.41) was required for calibration inside the software.

Figure 3.1 shows DLS size distribution by volume of non-deagglomerated nanodiamonds. It is easily seen that these nanodiamonds come aggregated up to microns ($\sim 4\mu\text{m}$) in size and are not suitable as a nano-luminescent thermal probe and also are present as a polydisperse sample. These are reasons for a deagglomeration method that both ensures a monodisperse sample and time efficient.

After applying the deagglomeration method, see Figure 3.2, nanodiamonds resulted in 164.2 nm in diameter size for at least 27% of the sample. It is clear that the Deagglomeration Method proposed is efficient yielding monodisperse samples. Comparing Figures 3.1 and 3.2, we can identify that the deagglomeration happens separating nanodiamonds from microns down to nanometers without the use of an external particle assisting the process.

Figure 3.3 illustrates Zeta potential distribution for the deagglomerated nanodiamonds, showing an apparent peak at ~ -20 mV.

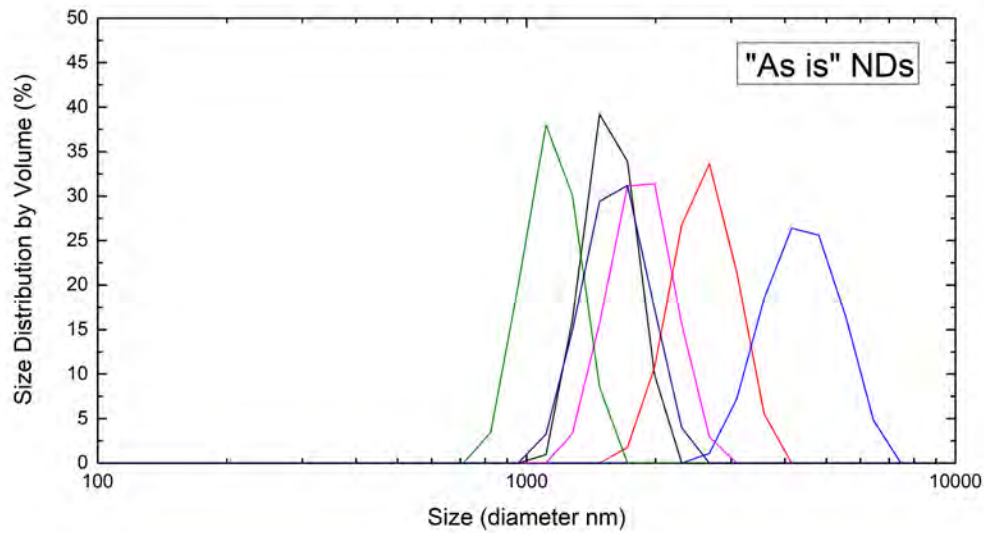


FIGURE 3.1: Nanodiamonds from Sigma Aldrich without the deagglomeration method. All these spectra are from the same sample, showing no apparent mean size over time. It is easily seen that these agglomerates are up to $8 \mu\text{m}$ in size and it comes as a polydisperse sample.

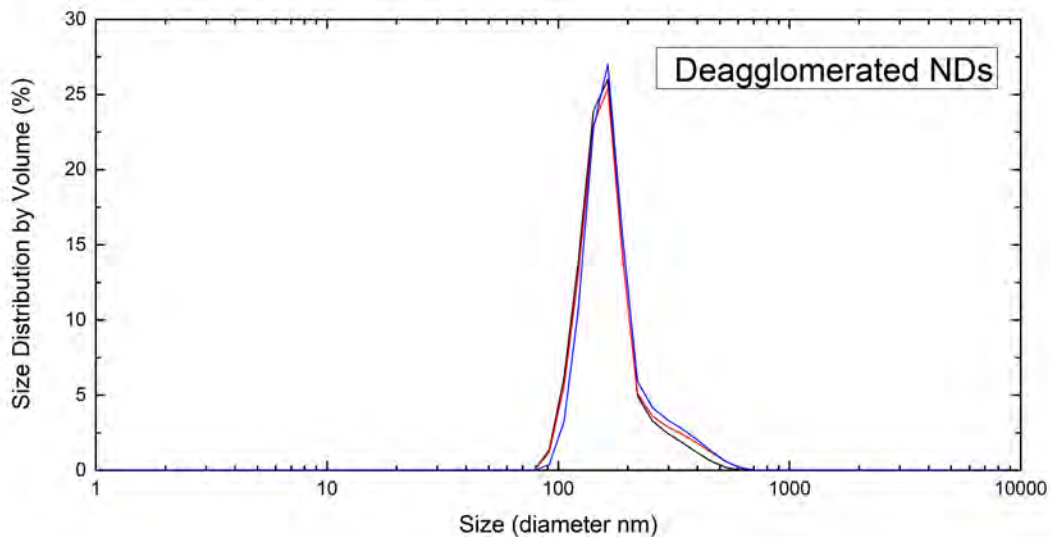


FIGURE 3.2: Size distribution by Volume of nanodiamonds after Deagglomeration Method. Three runs were done to observe the ND's hydrophobic radius of an average $R_H = 214.8 \text{ nm}$ and a PDI of 0.138.

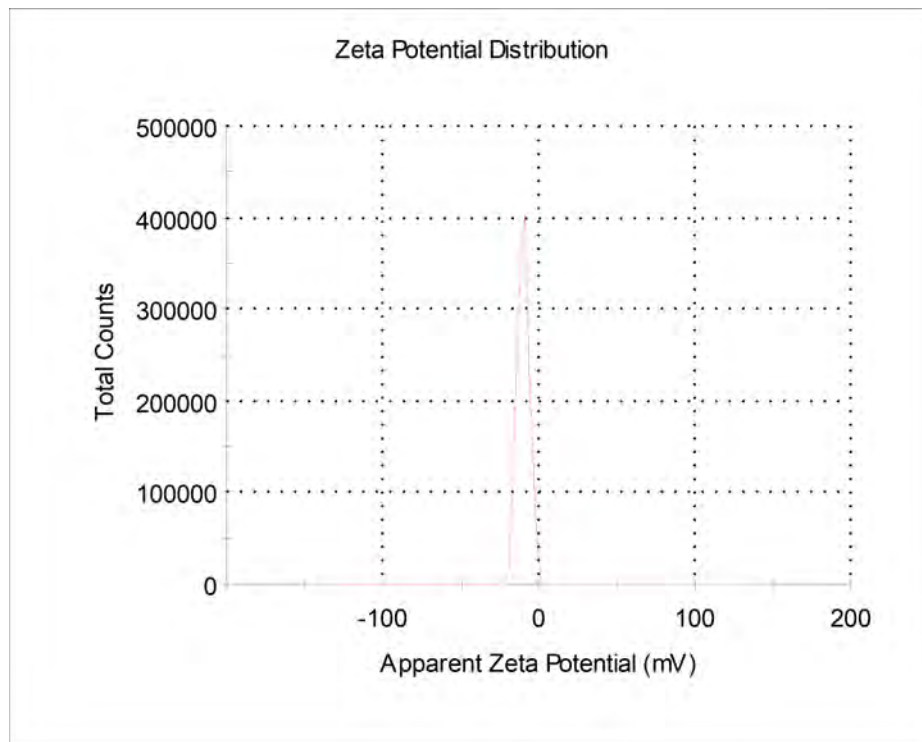


FIGURE 3.3: Graph of zeta potential analysis for nanodiamonds in aqueous solution. The peak corresponds to -20 mV.

3.3.2 Transmission Electron Microscopy

Transmission Electron Microscopy is a characterization technique that provides the morphology of the sample in micrographs over the nanometer range. This technique is mainly exploited to identify sample sizes and morphology.

All the measurements were carried on a Transmission Electron Microscope (TEM) JEOL JEM2010F (Field Emission) with a CCD camera Gatan SC200B. Acceleration voltage was stabilized at 200 kV throughout measurements. All data coming from the microscope was of raw type, this was handled using the software ImageJ to add scale bars to images.

Briefly, sample preparation was carried as follows:

1. NDs were re-sonicated following the steps in section 3.2 to assure size distribution.
2. A 1 mL sample was taken from each and put inside an eppendorf.

3. A TEM grid is necessary to mount the sample into the microscope, a support film from Ted Pella, Inc. (Prod. No. 01844-F) made out of Carbon and Copper was disposed to mount the sample.
4. Samples were taken to TEM for analysis.

Bright field images were obtained for the NDs sample. Below the images obtained from TEM apparatus. The images were taken in Bright Field (576x576 nm).

The sample was deagglomerated and small nanodiamonds were of an expectation. Figure 3.4 shows a diamond aggregate of smaller nanodiamonds that measures around 500 nm, illustrating how even though a deagglomeration method was carried, nanodiamonds keep sticking and forming larger aggregates, thus an efficient and time saving deagglomeration method.

After searching the sample, a nanodiamond of 200 nm of size was spotted. Figure 3.5 shows this nanodiamond and how even smaller nanodiamond pieces are stucked forming the former larger aggregate.

Figures 3.6 and 3.7 show a roughly 100 nm nanodiamond that has an even smaller nanodiamond (around 20 nm) stucked to its surface. These three figures serve as a marker of the agglomeration and deagglomeration process involved in nanodiamonds. A closer look of the nanodiamond is seen in Figure 3.8. A corroboration of size and morphology was achieved, while understanding that some nanodiamond agglomeration happened while preparing the sample for observation.

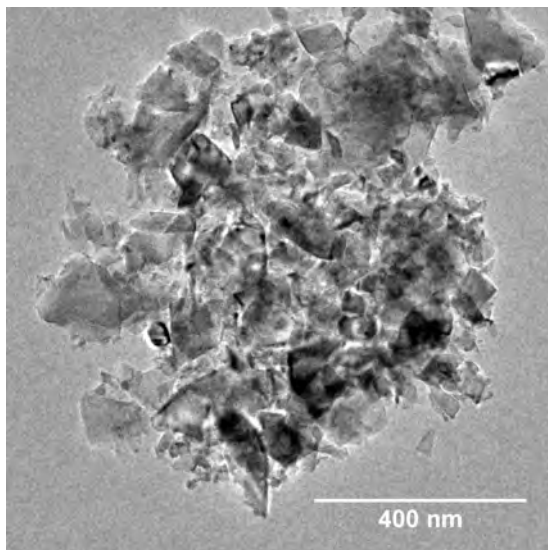


FIGURE 3.4: Aggregated nanodiamonds up to 500 nm.

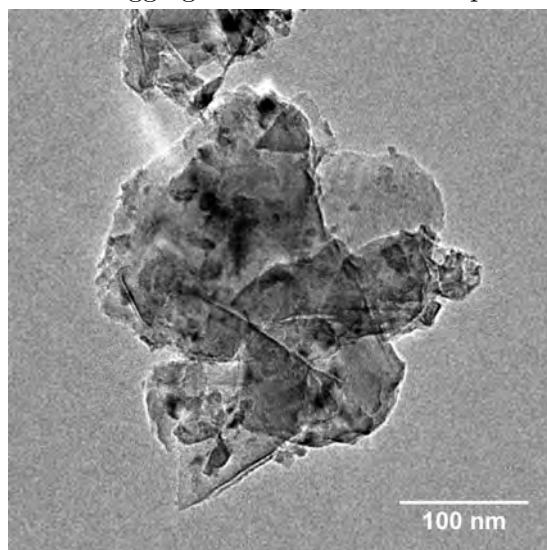


FIGURE 3.5: Aggregated nanodiamonds up to 200 nm.

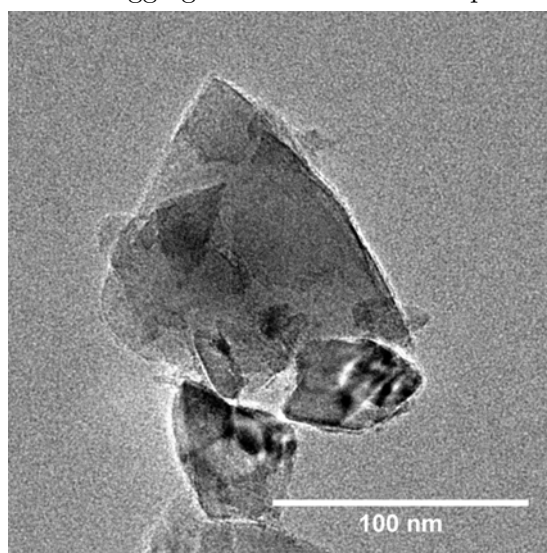


FIGURE 3.6: A nanodiamond. Smaller nanodiamonds can be found at the perimeter of the bigger nanodiamond.

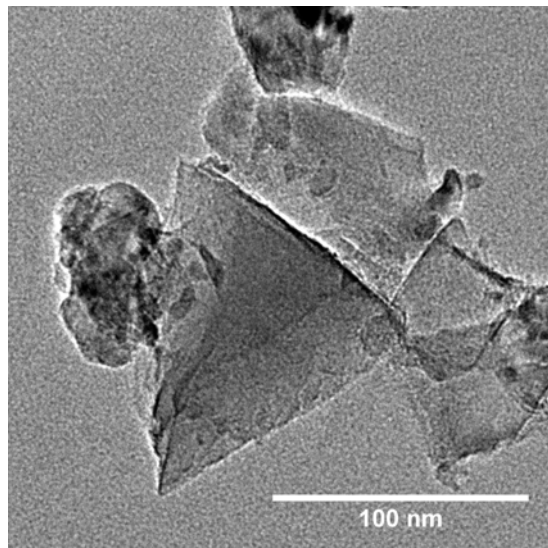


FIGURE 3.7: A 100 nm nanodiamond presenting similar features as the above. Smaller diamond shards can be seen as small as 30 nm.

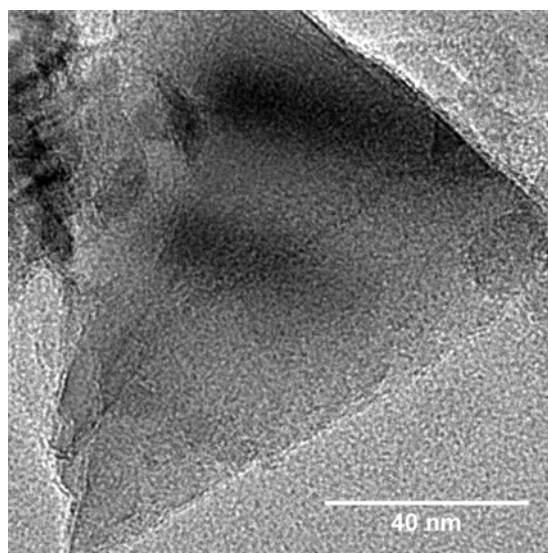


FIGURE 3.8: A closer inspection of the nanodiamond.

3.3.3 Confocal Fluorescence Microscopy

A Confocal Microscope Olympus BX41 equipped with a 488 nm Argon laser excitation source was used to obtain the fluorescence spectra of nanodiamonds at each run for each temperature. Temperature changes were done using a heating plate, heating the sample of stock nanodiamonds and using a single drop of the liquid in a sample holder to quickly measure its fluorescent signal. It can be observed that temperature changes (in this case 5°C) affect the fluorescent signal coming from the NV centers even at low temperatures (20°C to 60°C).

All spectra were recorded and normalized to the peak wavelength. Both NV complex's ZPLs (NV^0 and NV^-) are localized in 575 nm and 638 nm, respectively.

Figure 3.9 shows the Fluorescent spectra recorded for each temperature run of the nanodiamonds. It is known that the NV color center has two charge states: one at 575 nm (NV^0) and other at 638 (NV^-). These charge states can be determined directly by seeing the spectrum and provide direct evidence of the presence of NV color centers as their position correspond accordingly.

Figures 3.10 and 3.11 detail the zoom in the working window of each zero phonon line of each charge state. Spectral artifacts are seen easier and are to be quantified with the method proposed in section 2.3.6.

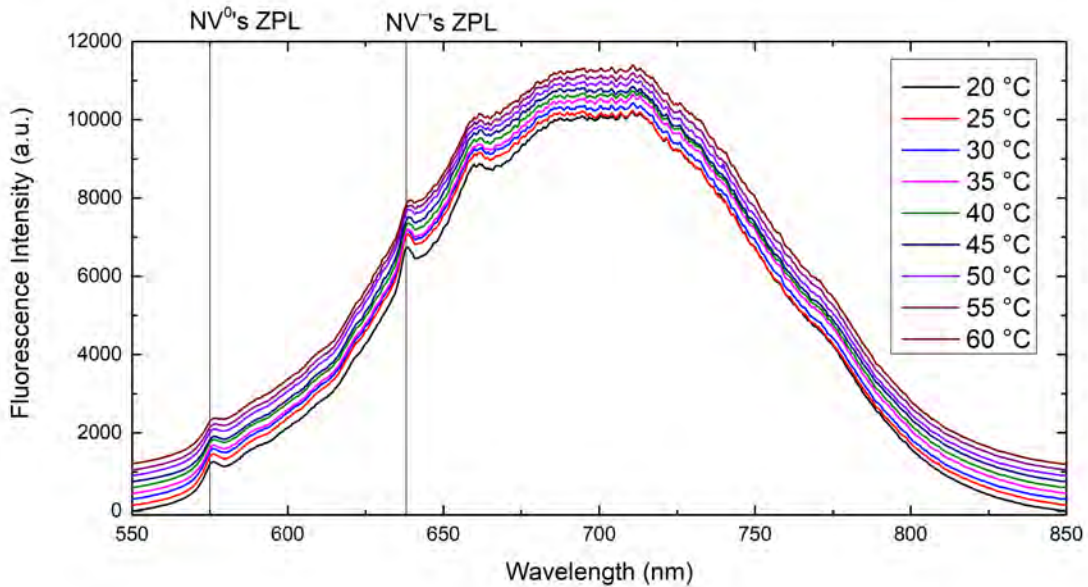


FIGURE 3.9: Fluorescent spectra of Stock Nanodiamonds at different temperatures. Changes due to temperature are seen in the NV emission lines. It is seen as well that there is no evident signal of how to correlate each ZPL to measure temperature.

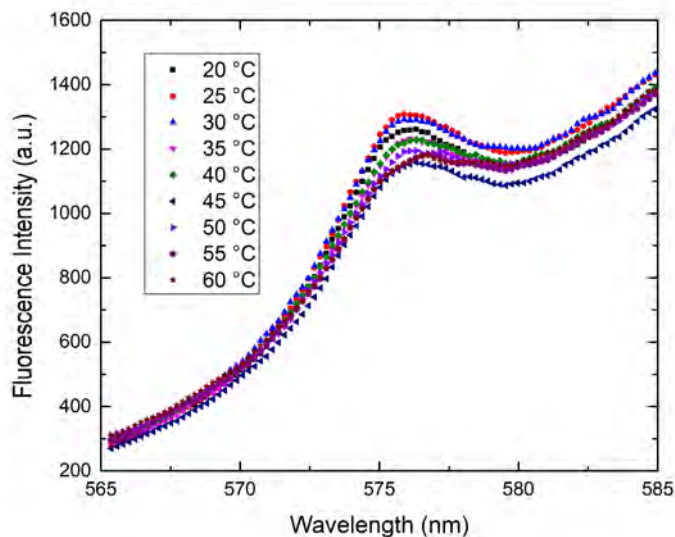


FIGURE 3.10: A detailed look of NV⁰'s ZPL over temperature changes.

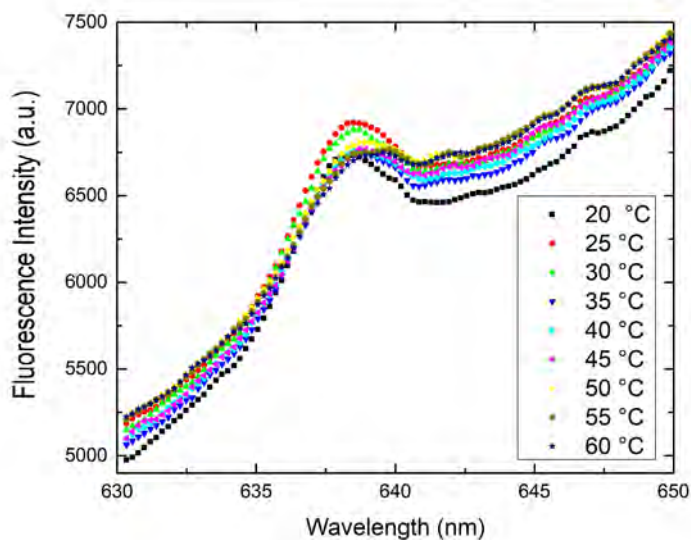


FIGURE 3.11: A detailed look of NV⁻'s ZPL over temperature changes.

3.4 Fluorescent Thermometry

A procedure similar to that of Plathotnik et al. was introduced in section 2.1. The method consists in accounting for two types of noise mentioned in section 2.3.4: Dark Current Noise and Photon Noise arising from the ND's NV center emission and do not correspond to static

parameters over temperature changes. Each NV charge state ZPL was worked around a 20 nm window. As each spectra is characterized by a set of parameters, we can reconstruct the scatter data with the fitted curve. Curve fitting and data handling was achieved with Origin-Pro 9.0 under the Non-Linear Fit feature with a customized non linear function as mentioned.

This was completed using Fitting Function Builder. Parameters are set inside the builder and equation 2.1 is expressed explicitly, considering none of the parameters as constant. χ^2 values are calculated inside the builder according to the expression 2.2 and are displayed within the data output.

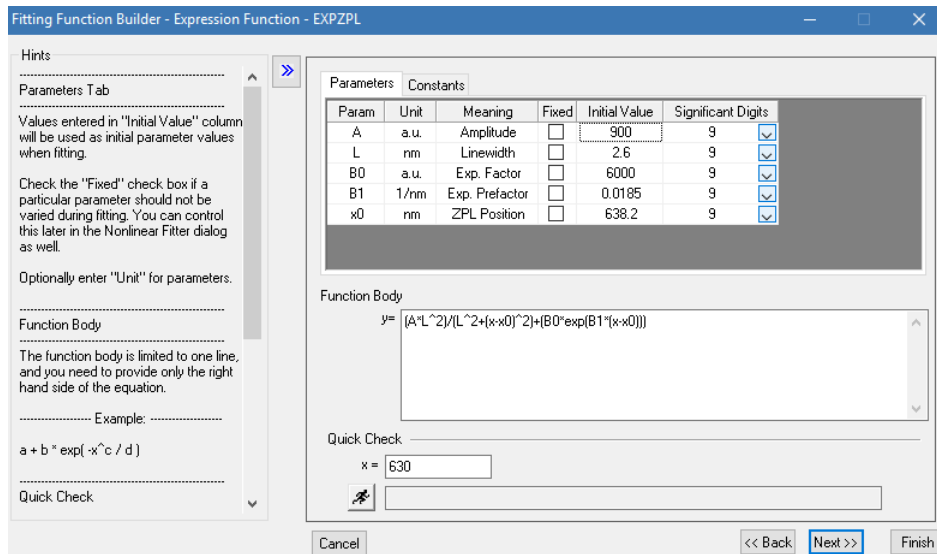


FIGURE 3.12: Fitting Function Builder. Parameters' initial values can be adjusted to further decrease number of iterations and/or increase fitting quality.

All the fluorescent spectra were analyzed according to Figure 3.12 within Origin software. Each charge state's fluorescent spectra (Figures 3.10 and 3.11) were arranged separately. This analysis yielded a corresponding set of numerical values (arranged in a table) for the parameters mentioned in equation 2.1 for each analyzed spectra. Each set of parameters for a given temperature corresponds to a curve fit for either charge state.

As each spectra corresponds to a set of parameters describing a curve, an arrangement of each spectra and their corresponding fit is shown in Figure 3.13 for the NV^0 charge state and in Figure 3.14 for the NV^- charge state. It can be seen that both curve fits are of the same kind as it comes from the same methodology but differ in numerical values.

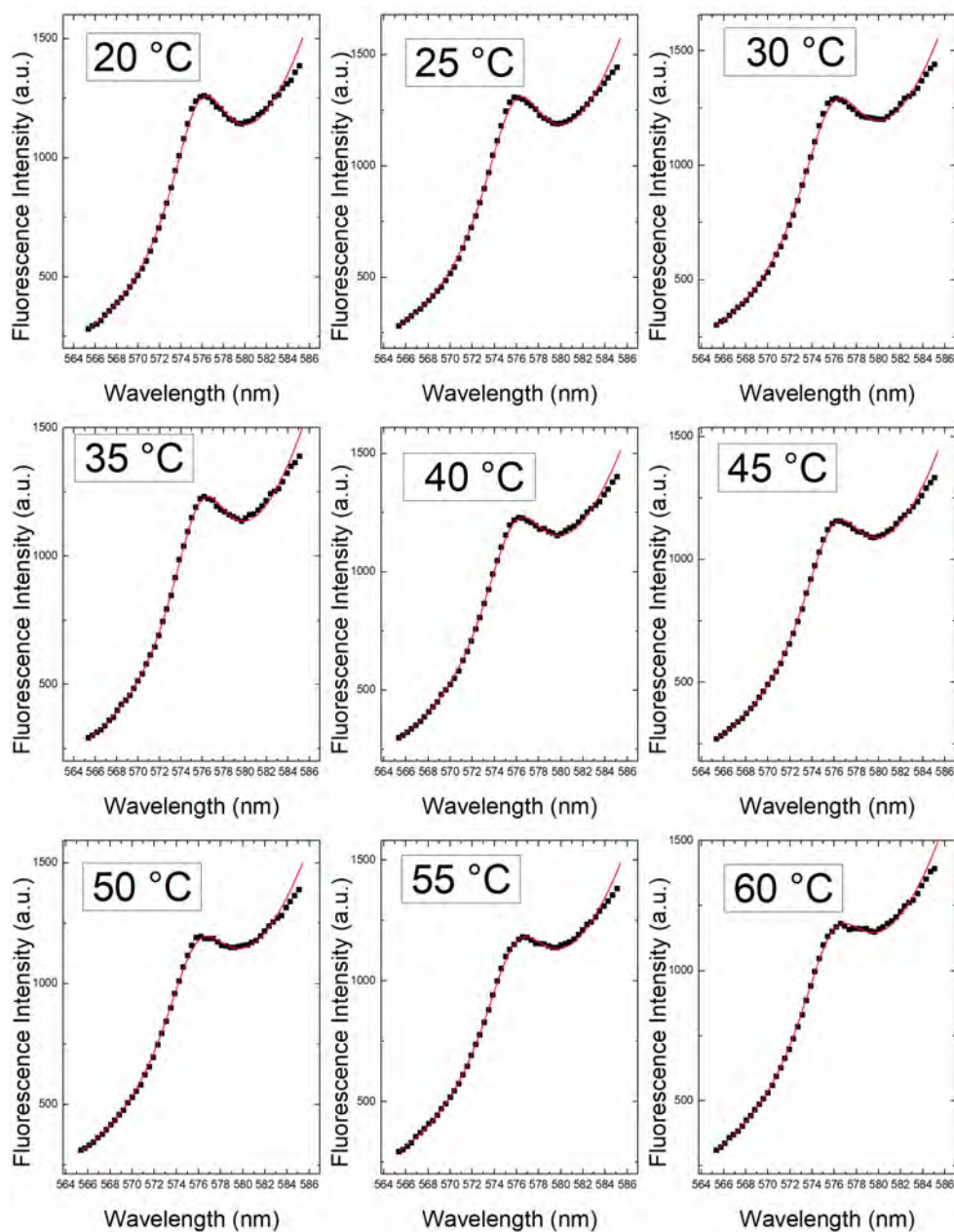


FIGURE 3.13: All fitted spectra for NV^0 charge state. The vertical axis corresponds to Fluorescence Intensity from 200 to 1600 a.u. and horizontal axis is the wavelength from 564 to 587 nm.

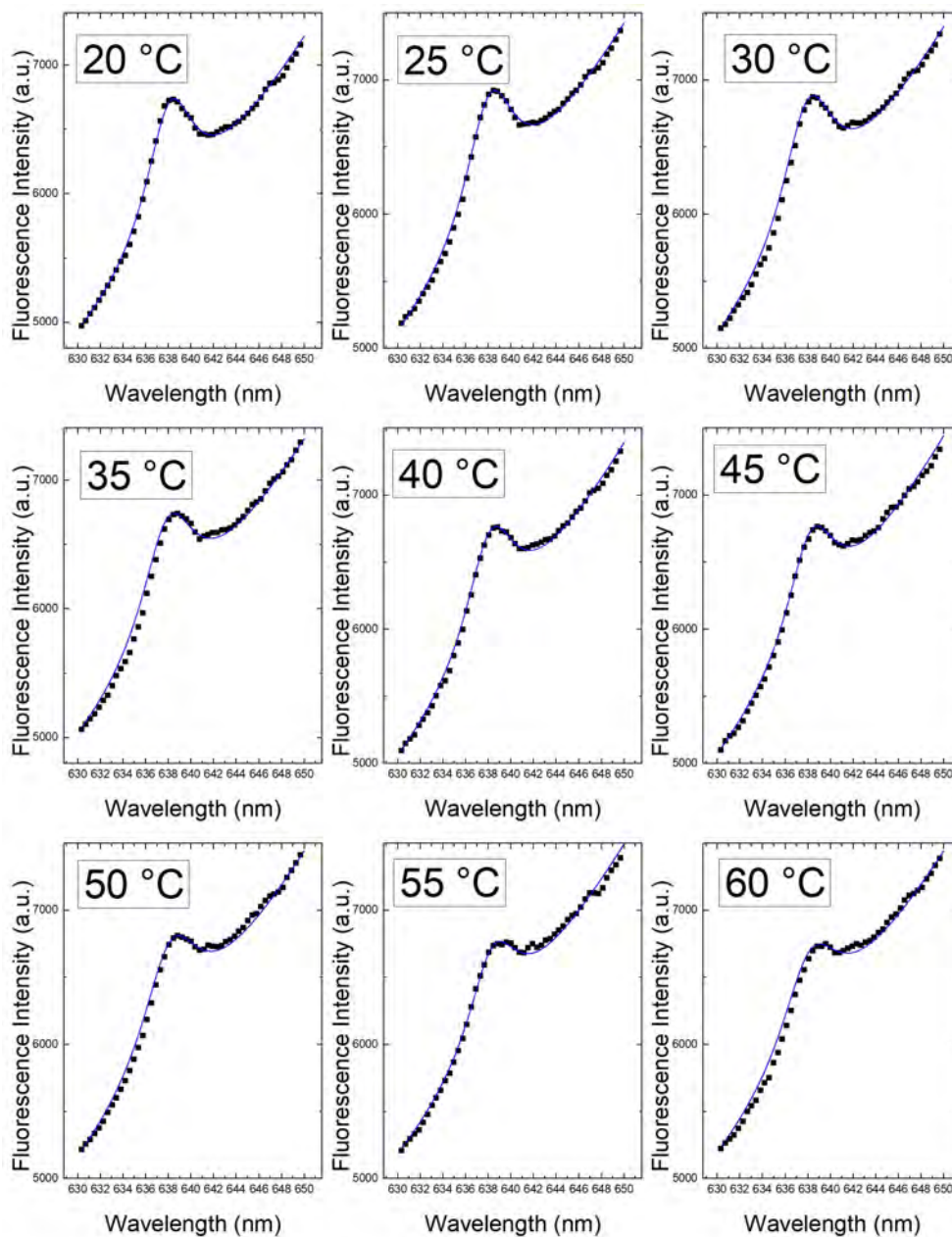


FIGURE 3.14: All fitted spectra for NV^- charge state. The vertical axis corresponds to Fluorescence Intensity from 5000 to 7500 a.u. and horizontal axis is the wavelength from 628 to 651 nm.

3.4.1 Tables of Parameters

Following the steps mentioned a table of parameters versus temperature can be arranged. This was done for both NV charge states (NV^0 and NV^-). Chi squared value is given for

the batch analysis as well as the coefficient of determination (R^2). For best fitting results χ^2 should tend to 0 while $COD(R^2)$ should tend to 1, which is the case for a perfect fit.

T (°C)	Rel. Amplitude (A)	Linewidth (Γ)	B_0	B_1	ZPL Position (x_0)
20	680.894	3.665067	564.3142	0.096108	575.8033
25	720.6046	3.72637	572.1231	0.099549	575.831
30	685.2764	3.913429	587.9281	0.095219	575.8433
35	630.8624	3.66655	583.1144	0.09351	575.8515
40	624.5284	3.881079	585.6648	0.093043	575.8444
45	588.0182	3.814893	552.303	0.094903	575.882
50	568.8835	3.986644	603.21	0.089433	575.8763
55	569.9526	3.972699	590.25	0.091318	575.9238
60	541.2813	4.056245	614.4128	0.088097	575.9262

FIGURE 3.15: Parameter table for NV^0 ZPL. Reduced $\chi^2=0.10229345$ and $COD(R^2)=0.99999943$

T (°C)	Rel. Amplitude (A)	Linewidth (Γ)	B_0	B_1	ZPL Position (x_0)
20	1034.419	2.61417	5682.449	0.01969	638.1268
25	1027.215	2.72488	5871.487	0.01925	638.1534
30	1055.328	3.03783	5797.797	0.01897	637.9088
35	968.0776	2.94696	5745.284	0.01945	638.0153
40	934.1154	2.95707	5797.977	0.01932	638.0735
45	924.4801	3.06005	5809.625	0.01948	638.1023
50	838.9046	2.9549	5936.87	0.01899	638.3127
55	823.2157	3.21156	5902.83	0.01868	638.1322
60	722.3613	2.87054	5988.158	0.01876	638.4308

FIGURE 3.16: Parameter table for NV^- ZPL. Reduced $\chi^2=0.18490612$ and $COD(R^2)=0.99999998$.

These parameters are obtained after fitting the curve mentioned in equation 2.1 and minimizing Chi-Squared function.

3.4.2 Thermometric Scales

The thermometric scales are built upon the parameters obtained from tables shown before for each charge state. Consequently statistical markers show a tendency for χ^2 to 0 and $COD(R^2)$ to 1. This validates the curve proposal as an excellent emission fitting and thus allows to further investigate thermometric properties within the obtained parameters. A Linear Fit was made to each column shown in Figure 3.15 and 3.16 and is illustrated in each thermometric scale with its R^2 value shown in the caption.

NV⁰'s Thermometric Scales

The relative amplitude was the parameter that best predicted temperature showing the best linear tendency for all thermometric scales for this charge state. Linewidth thermometric scale showed a linear correspondance but wasn't as good as relative amplitude but provided evidence of bolder vibrational levels with increasing temperature. The NV⁰ ZPL position didn't predict temperature as this parameter remained nearly static.

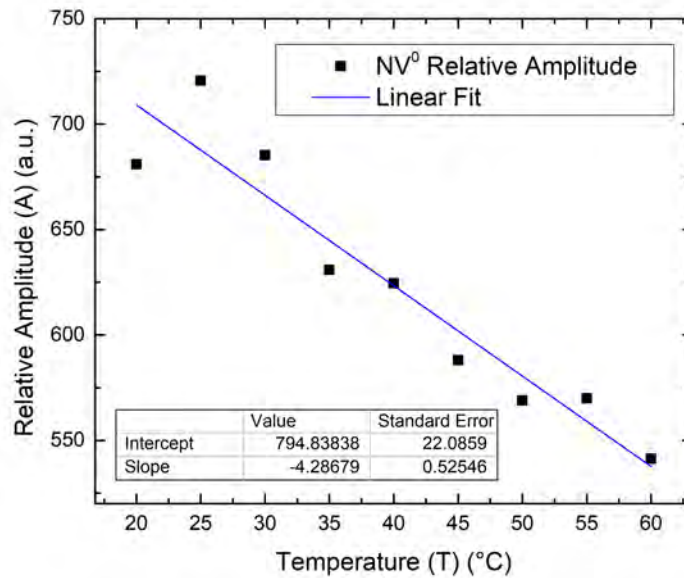


FIGURE 3.17: Relative amplitude (A) thermometric scale for NV⁰'s zero-phonon line ($R^2=0.99124$). Over increasing temperature changes A decreases in fluorescence intensity.

Over increasing temperature the relative amplitude decreases. A less intense fluorescent signal is then expected as temperature rises, which corresponds to a lower emission rate for this charge state.

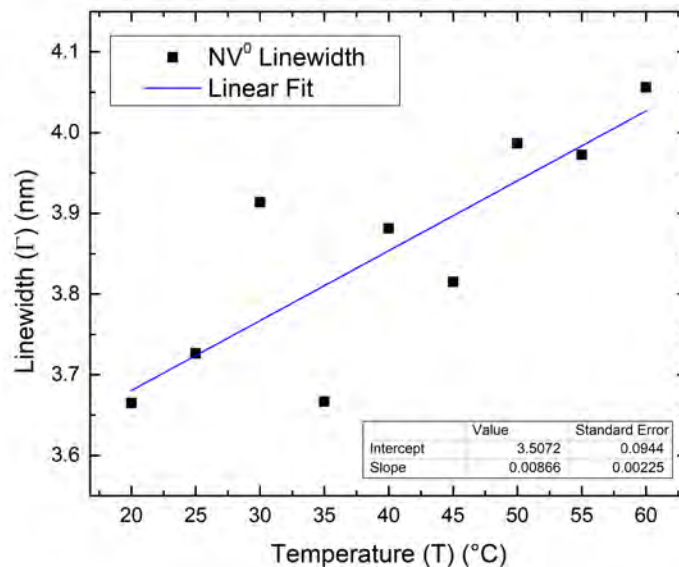


FIGURE 3.18: Linewidth (Γ) thermometric scale for NV^0 's zero-phonon line ($R^2=0.83423$).

The linewidth shows a decent fit but also presents some noise (see Figure 3.17, 30° and 35°).

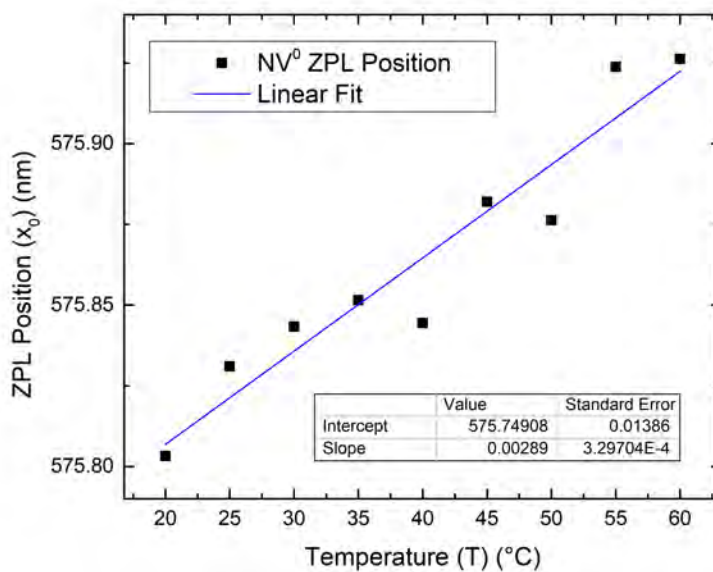


FIGURE 3.19: NV^0 's ZPL position thermometric scale ($R^2=0.94451$).

The ZPL position changed very little over temperature changes, this thermometric scale shows a good fit but doesn't provide much information as the changes in positions are very little to account for.

NV^- 's Thermometric Scales

For the NV^- charge state it is found that relative amplitude parameter is the best for temperature measurements. A notably increase in linear correlation was found for the linewidth parameter allowing for a better linear fitting than that of NV^0 and a similar static ZPL position was observed.

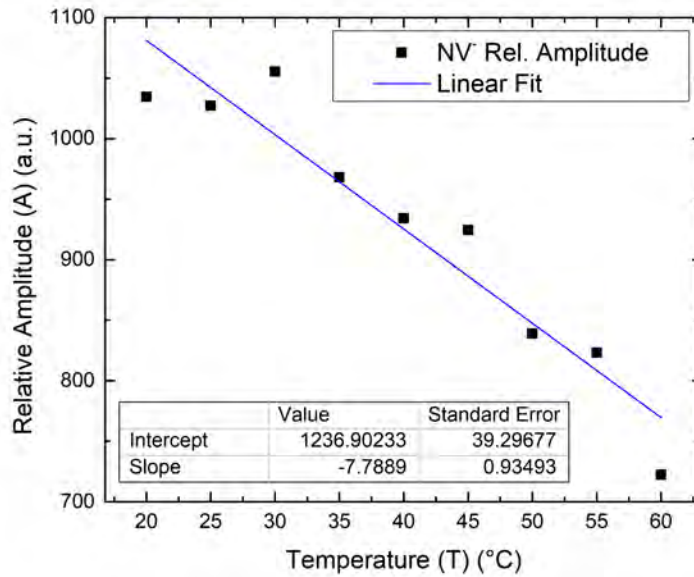


FIGURE 3.20: Relative amplitude (A) thermometric scale for NV^- 's zero-phonon line ($R^2=0.9953$).

The relative amplitude thermometric scale shows a decreasing intensity as temperature rises.

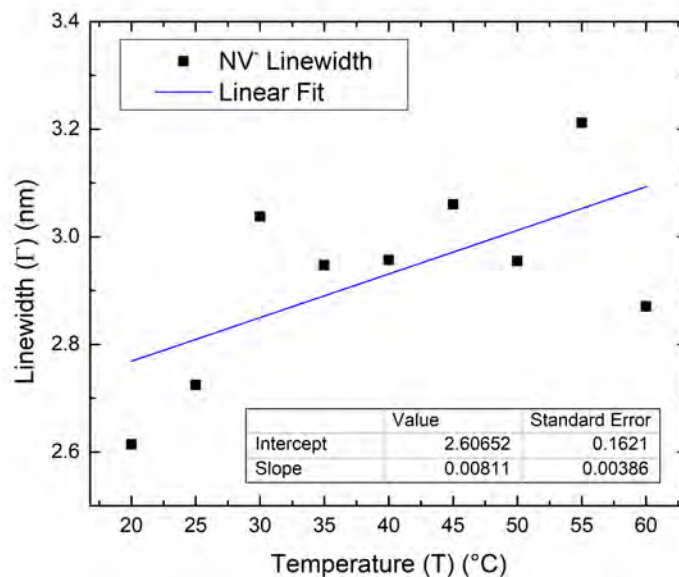


FIGURE 3.21: Linewidth (Γ) thermometric scale for NV^- 's zero-phonon line ($R^2=0.89956$).

The linewidth of this charge state increases with increasing temperature, meaning bolder energy levels within the electronic structure.

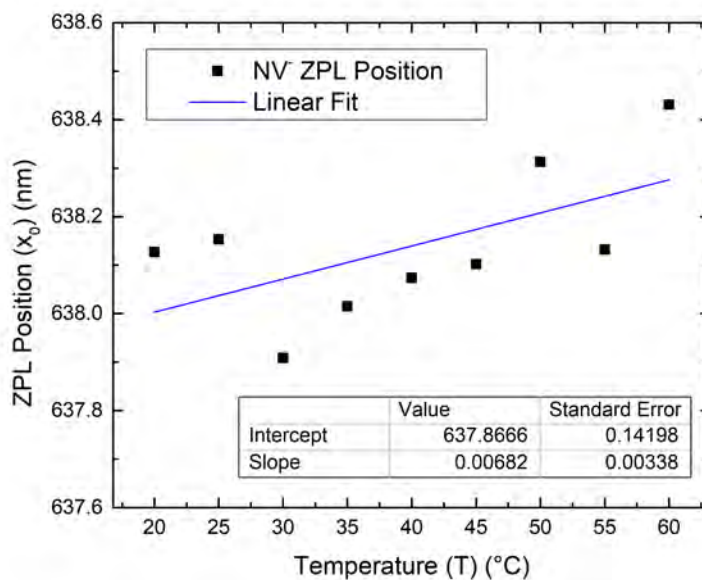


FIGURE 3.22: NV^0 's ZPL position thermometric scale ($R^2=0.87798$).

Summarizing, background noise parameters (B_0 and B_1) aren't a good markers for thermometry as these won't provide information about the sample local temperature. In the other hand, the parameters A , Γ and x_0 are promising as these describe the emission curve of the fluorescent spectra. We can evidence how these factors are changing over temperature changes and how they correlate to temperature.

- **Relative Amplitude:** This amplitude tends to decrease as temperature increases, thus less intensity of photons in being emitted by the centers as higher surrounding temperature is present. The inverse phenomenon is observed while temperature decreases.
- **Linewidth:** The spectral emission window for the ZPL of each charge state gets wider as temperature increases and sharper as temperature decreases.
- **ZPL Position:** This value remained nearly constant, their thermometric scales show little to no movement and their slope (sensibility) is nearly zero. This evidences how these energy levels remain constant even for temperature changes.

Chapter 4

Conclusions

In this work, for the first time, nanodiamonds in solution were successfully used as temperature sensors based in their fluorescence, distinguishing further from the literature. Nanodiamond agglomeration was studied too by means of DLS technique to ensure size in all the confocal microscope runs. Agglomeration happens over time and it was easily seen that a two day storage agglomerates nanodiamonds up to sizes of 500 nm; therefore, a Deagglomeration Method was adapted from Pedroso-Santana et al. [167], where they used nanodiamonds in powder in a Bead Assisted Sonic Disintegration, mixing the nanodiamonds with silica beads in the sonicating process. These authors report silica beads synthesis, sonication times with possible sonicator settings to ensure size reduction and an overview of the nanodiamond platform from pH adjustment for non-cytotoxicity, to a carboxylation procedure to achieve surface functionalization for biomedical purposes. The Deagglomeration Method shown in this thesis was crafted in the sense of consistent sonication times; removing the silica beads using only "as is" nanodiamonds, and to ensure size reduction in the order of nanometers. Size distribution showed that the nanodiamonds' size are in average 180 nm as a monodisperse sample with a small amount with sizes <100 nm. The Deagglomeration Method proves to be cost, time and size reduction effective.

Consistent sizes (and also shape) were corroborated by TEM technique. This technique provided electron images where nanodiamonds can be seen in the nanometer range. Images show smaller nanodiamonds (some of 30 nm) agglomerating to the average size but mostly show nanodiamonds in the size range of 100 nm. This result contrasts with DLS measurements as deagglomerated nanodiamonds are still agglomerated by smaller nanodiamonds, thus, the Deagglomeration Method proposed ensures size control and could be adapted further to ensure size reduction. As nanodiamonds are in solution, they could be easily integrated into tissues.

After this characterization, a fluorescent spectroscopy technique was carried out at room temperature to locate both charge states of the NV color center serving as a marker to formalize a fluorescent thermometry method. The nanodiamonds used in this work have 800 NV centers per particle concentration and were of choice as they present the best fluorescent signal; greater than those of 300 or 15 NV center per particle. Briefly, 3 effective parameters (A , Γ and x_0 , photon noise) and 2 auxiliary background parameters (B_0 and B_1 , background noise) are the foundation to account for changes in fluorescence intensity over temperature changes. This allowed for a general observation of Intensity features over temperature changes. This were later minimized using χ^2 function which yielded a near-zero value for both charge states of the color center. From the 5 parameters, two are for the background noise and don't provide information about temperature as they only account for a static background noise over temperature changes; nonetheless, the three remaining parameters describe how the ZPL behaves as temperature changes. These 3 parameters' response over temperature for each charge state was similar: their relative amplitude decreased, their linewidth increased and their ZPL position remained nearly static with increasing temperature, effectively describing bolder energy levels with increasing temperature. It is found that the best fit is the NV^- charge state's relative amplitude, corresponding to the best thermometric scale. Each linewidth for each charge state doesn't change more than 0.5 nm over the whole process and the ZPL position moves ever so slightly to be able to account for temperature measurements.

In the biological sense: metabolism, cancer or even altered metabolic states increase or decrease temperature so a sensitive enough probe is required to account for a specific change in temperature. As the Relative Amplitude parameter relates to light intensity directly a possible biomarker application could be of use.

Overall, carbon-like materials show promise for biomedical applications. In this thesis, stable thermometric scales were successfully built upon the fluorescent nanodiamonds spectrum. This set up is different from other luminescent rare-earth nanoparticles or quantum dots as these nanodiamonds possess great surface functionalization with non-cytotoxic properties serving as biomarkers to describe local thermal motion. A more described work could be applied in the field of internalizing functionalized nanodiamonds in solution into a cell to further revise its thermometry performance and internalization mechanism.

Bibliography

- [1] Childs, P. R. N. (2016). Thermometry at the Nanoscale. <https://doi.org/10.1039/9781782622031>
- [2] C. F. Chapman, Y. Liu, G. J. Sonek and B. J. Tromberg, The use of exogenous fluorescent probes for temperature measurements in single living cells, *Photochem. Photobiol.*, 1995,62, 416–425.
- [3] O. Zohar, M. Ikeda, H. Shinagawa, H. Inoue, H. Nakamura, D. Elbaum, D. L. Alkon and T. Yoshioka, Thermal imaging of receptor-activated heat production in single cells, *Biophys. J.*, 1998,74, 82–89.
- [4] M. Suzuki, V. Tseeb, K. Oyama and S. Ishiwata, Microscopic detection of thermogenesis in a single HeLa cell, *Biophys. J.*, 2007,92, L46–L48.
- [5] N. Mohan, C. S. Chen, H. H. Hsieh, Y. C. Wu and H. C. Chang, In vivo imaging and toxicity assessments of fluorescent nanodiamonds in *Caenorhabditis elegans*, *Nano Lett.*, 2010,10, 3692–3699.
- [6] C. Gota, K. Okabe, T. Funatsu, Y. Harada and S. Uchiyama, Hydrophilic fluorescent nanogel thermometer for intracellular thermometry, *J. Am. Chem. Soc.*, 2009,131, 2766–2767.
- [7] H. Huang, S. Delikanli, H. Zeng, D. M. Ferkey and A. Pralle, Remote control of ion channels and neurons through magnetic-field heating of nanoparticles, *Nat. Nanotechnol.*, 2010,5, 602–606.
- [8] J. M. Yang, H. Yang and L. W. Lin, Quantum dot nano thermometers reveal heterogeneous local thermogenesis in living cells, *ACS Nano*, 2011, 5, 5067–5071.
- [9] K. Okabe, N. Inada, C. Gota, Y. Harada, T. Funatsu and S. Uchiyama, Intracellular temperature mapping with a fluorescent polymeric thermometer and fluorescence lifetime imaging microscopy, *Nat. Commun.*, 2012, 3, 705. Multifunctional Luminescent Platforms for Dual-sensing 505

-
- [10] C.L. Wang, R.Z. Xu, W.J. Tian, X.L. Jiang, Z.Y. Cui, M. Wang, H.M. Sun, K. Fang and N. Gu, Determining intracellular temperature at single-cell level by a novel thermocouple method, *Cell Res.*, 2011,21, 1517–1519.
- [11] P. Neumann, I. Jakobi, F. Dolde, C. Burk, R. Reuter, G. Waldherr, J. Honert, T. Wolf, A. Brunner, J. H. Shim, D. Suter, H. Sumiya, J. Isoya and J. Wrachtrup, High-precision nanoscale temperature sensing using single defects in diamond, *Nano Lett.*, 2013,13, 2738–2742.
- [12] G. Kucsko, P. C. Maurer, N. Y. Yao, M. Kubo, H. J. Noh, P. K. Lo, H. Park and M. D. Lukin, Nanometre-scale thermometry in a living cell, *Nature*, 2013, 500, 54–58.
- [13] A. T. Jonstrup, J. Fredsoe and A. H. Andersen, DNA hairpins as temperature switches, thermometers and ionic detectors, *Sensors*, 2013, 13, 5937–5944.
- [14] R. Schirhagl, K. Chang, M. Loretz and C. L. Degen, Nitrogen-vacancy centers in Diamond: nanoscale sensors for physics and biology, *Annu. Rev. Phys. Chem.*, 2014,65, 83–105.
- [15] P. Kolodner and J. A. Tyson, Remote thermal imaging with 0.7mm spatial resolution using temperature-dependent fluorescent thin films, *Appl. Phys. Lett.*, 1983,42, 117–119.
- [16] L. Aigouy, G. Tessier, M. Mortier and B. Charlot, Scanning thermal imaging of micro-electronic circuits with a fluorescent nanoprobe, *Appl. Phys. Lett.*, 2005,87(18), 184105.
- [17] G. Tessier, M. Bardoux, C. Boue and D. Fournier, Back side thermal imaging of integrated circuits at high spatial resolution, *Appl. Phys. Lett.*, 2007, 90, 171112.
- [18] W. J. Liu and B. Z. Yang, Thermography techniques for integrated circuits and semiconductor devices, *Sens. Rev.*, 2007,27, 298–309.
- [19] W. Jung, Y. W. Kim, D. Yim and J. Y. Yoo, Microscale surface thermometry using SU8/Rhodamine-B thin layer, *Sens. Actuators, A*, 2011,171, 228–232.
- [20] H. B. Mao, T. L. Yang and P. S. Cremer, A microfluidic device with a linear temperature gradient for parallel and combinatorial measurements, *J. Am. Chem. Soc.*, 2002,124, 4432–4435.
- [21] R. Samy, T. Glawdel and C. L. Ren, Method for microfluidic whole-chip temperature measurement using thin-film poly(dimethylsiloxane)/ rhodamine B, *Anal. Chem.*, 2008,80, 369–375.

- [22] C. Gosse, C. Bergaud and P. Low, Molecular probes for thermometry in microfluidic devices, in *Thermal Nanosystems and Nanomaterials*, Topics in Advanced Physics, ed. S. Volz, Springer-Verlag, Berlin, 2009, vol. 118, pp. 301–341.
- [23] T. Barilero, T. Le Saux, C. Gosse and L. Jullien, Fluorescent thermometers for dual-emission-wavelength measurements: molecular engineering and application to thermal imaging in a microsystem, *Anal. Chem.*, 2009,81, 7988–8000.
- [24] E. M. Graham, K. Iwai, S. Uchiyama, A. P. de Silva, S. W. Magennis and A. C. Jones, Quantitative mapping of aqueous microfluidic temperature with sub-degree resolution using fluorescence lifetime imaging microscopy, *Lab Chip*, 2010,10, 1267–1273.
- [25] J. Feng, K. J. Tian, D. H. Hu, S. Q. Wang, S. Y. Li, Y. Zeng, Y. Li and G. Q. Yang, A Triarylboron-based fluorescent thermometer: sensitive over a wide temperature range, *Angew. Chem., Int. Ed.*, 2011,50, 8072–8076.
- [26] M. J. Hartmann, Minimal length scales for the existence of local temperature, *Contemp. Phys.*, 2006,47(2), 89–102.
- [27] B. W. Mangum and G. T. Furukawa, Guidelines for realizing the ITS-90, NIST Tech, note 1265, 1990.
- [28] C.D.S. Brites, P.P. Lima, N.J.O. Silva, A. Millan, V.S. Amaral, F. Palacio and L. D. Carlos, Thermometry at the nanoscale, *Nanoscale*, 2012,4, 4799–4829.
- [29] M. E. Kose, B. F. Carroll and K. S. Schanze, Preparation and spectroscopic properties of a dual luminophore pressure sensitive paint, *Langmuir*, 2005b,21, 9121–9129.
- [30] M. E. Kose, A. Omar, C. A. Virgin, B. F. Carroll and K. S. Schanze, Principal component analysis calibration method for dual luminophore pressure sensitive paints, *Langmuir*, 2005b,21, 9110–9120.
- [31] N. Chandrasekharan and L. A. Kelly, A dual fluorescence temperature sensor based on perylene/excimer interconversion, *J. Am. Chem. Soc.*, 2001, 123, 9898–9899.
- [32] G. Walker, V. Sundar, C. Rudzinski, A. Wun, M. Bawendi and D. Nocera, Quantum-dot optical temperature probes, *Appl. Phys. Lett.*, 2003,83, 3555–3557.
- [33] H. Sakaue, A. Aikawa, Y. Iijima, T. Kuriki and T. Miyazaki, Quantum dots as global temperature measurements, in *Quantum Dots – A Variety of New Applications*, ed. A. Al-Ahmadi, In Tech ch. 7, 2012.

- [34] W.G.J.H.M. van Sark, P.L.T.M. Frederix, A.A. Bol, H.C. Gerritsen and A. Meijerink, Blueing, bleaching, and blinking of single CdSe/ZnS quantum dots, *Chem. Phys. Chem.*, 2002,3, 871–879.
- [35] M. Nakamura, S. Ozaki, M. Abe, T. Matsumoto and K. Ishimura, One-pot synthesis and characterization of dual fluorescent thiolorganosilica nanoparticles as non-photoblinking quantum dots and their applications for biological imaging, *J. Mater. Chem.*, 2011,21, 4689–4695.
- [36] M. J. Holmes, K. Choi, S. Kako, M. Arita and Y. Arakawa, Roomtemperature triggered single photon emission from a III-nitride sitecontrolled nanowire quantum dot, *Nano Lett.*, 2014,14(2), 982–986.
- [37] B. Somogyi and A. Gali, Computational design of in vivo biomarkers, *J. Phys.: Condens. Matter*, 2014,26, 143202.
- [38] A. L. Heyes, Thermographic phosphor thermometry for gas turbines, in *Advanced Measurement Techniques for Aero and Stationary Gas Turbines*, ed. C. H. Sieverding and J. F. Brouckaert, VKI LS 2004-04, 2004.
- [39] A. L. Heyes, On the design of phosphors for high temperature thermometry, *J. Lumin.*, 2009,129, 2004–2009.
- [40] Y. Cui, W. Zou, R. Song, J. Yu, W. Zhang, Y. Yang and G. Qian, A ratiometric and colorimetric luminescent thermometer over a wide temperature range based on a lanthanide coordination polymer, *Chem. Commun.*, 2014,50, 719–721.
- [41] W. Li, Z. J. Coppens, D. Greg Walker and J. G. Valentine, Electron beam physical vapor deposition of thin ruby films for remote temperature sensing, *J. Appl. Phys.*, 2013,113, 163509.
- [42] V. Lojpur, M. G. Nikolic, D. Jovanovic, M. Medic, Z. Antic and M. D. Dramicanin, Luminescence thermometry with Zn₂SiO₄:Mn²⁺ powder, *Appl. Phys. Lett.*, 2013,103, 141912.
- [43] L. Liu, S. Creten, Y. Firdaus, J. Jesus, A. Flores Cuautle, M. Kouyate, M. Van der Auweraer and C. Glorieux, Fluorescence spectra shape based dynamic thermometry, *Appl. Phys. Lett.*, 2014,104, 031902.

- [44] O. Yarimaga, S. Lee, D. Y. Ham, J. M. Choi, S. G. Kwon, M. Im, S. Kim, J.-M. Kim and Y.-K. Choi, Thermofluorescent conjugated polymer sensors for nano- and microscale temperature monitoring, *Macromol. Chem. Phys.*, 2011,212, 1211–1220.
- [45] F. Vetrone, R. Naccache, A. Zamarron, A. J. De La Fuente, F. Sanz-Rodriguez, L. M. Maestro, E. M. Rodriguez, D. Jaque and J. Garcia, Temperature sensing using fluorescent nanothermometers, *ACS Nano*, 2010,4, 3254–3258.
- [46] C. Paviolo, A. H. A. Clayton, S. L. McArthur and P. R. Stoddart, Temperature measurement in the microscopic regime: a comparison between fluorescence lifetime- and intensity-based methods, *J. Microsc.*, 2013, 250, 179–188.
- [47] K. M. McCabe and M. Hernandez, Molecular thermometry, *Pediatr. Res.*, 2010, 67, 469–475.
- [48] Q. Fu, G. V. R. Rao, L. K. Ista, Y. Wu, B. P. Andrzejewski, L. A. Sklar, T. L. Ward and G. P. Lopez, Control of molecular transport through stimuli-responsive ordered mesoporous materials, *Adv. Mater.*, 2003,15, 1262–1266.
- [49] E. Aznar, L. Mondragon, J. V. Ros-Lis, F. Sancenon, M. D. Marcos, R. Martinez-Manez, J. Soto, E. Perez-Paya and P. Amoros, Finely tuned temperature-controlled cargo release using paran-capped mesoporous silica nanoparticles, *Angew. Chem., Int. Ed.*, 2011,50, 11172–11175.
- [50] P. Neumann, I. Jakobi, F. Dolde, C. Burk, R. Reuter, G. Waldherr, J. Honert, T. Wolf, A. Brunner, J. H. Shim, D. Suter, H. Sumiya, J. Isoya and J. Wrachtrup, High-precision nanoscale temperature sensing using single defects in diamond, *Nano Lett.*, 2013,13, 2738–2742.
- [51] P. Bon, N. Belaid, D. Lagrange, C. Bergaud, H. Rigneault, S. Monneret and G. Baou, Three-dimensional temperature imaging around a gold microwire, *Appl. Phys. Lett.*, 2013,102, 244103.
- [52] G. Binnig, H. Rohrer, C. Gerber and E. Weibel, Tunneling through a controllable vacuum gap, *Appl. Phys. Lett.*, 1982,40, 178–180.
- [53] A. Majumdar, J. P. Carrejo and J. Lai, Thermal imaging using the atomic force microscope, *Appl. Phys. Lett.*, 1993,62, 2501–2503.
- [54] G.Mills,H.Zhou,A.Midha,L.DonaldsonandJ.M.R.Weaver,Scanning thermal microscopy using batch fabricated thermocouple probes, *Appl. Phys. Lett.*, 1998,72, 2900–2902.

- [55] A. Hammiche, M. Reading, H. M. Pollock, M. Song and D. J. Hourston, Localized thermal analysis using a miniaturized resistive probe, *Rev. Sci. Instrum.*, 1996,67, 4268–4274.
- [56] P.G. Royall, V.L.Kett, C.S.Andrews and D.Q.M. Craig, Identification of crystalline and amorphous regions in low molecular weight materials using microthermal analysis, *J. Phys. Chem. B*, 2001,105, 7021–7026.
- [57] S. Lefevre and S. Volz, 3o-scanning thermal microscope, *Rev. Sci. Instrum.*, 2005,76, 033701.
- [58] Y. H. Gao and Y. Bando, Carbon nanothermometer containing gallium, *Nature*, 2002,415, 599.
- [59] C. Y. Wang, N. W. Gong and L. J. Chen, High sensitivity solid state Pb(core)/ZnO(shell) nanothermometers fabricated with a facile galvanic displacement method, *Adv. Mater.*, 2008,20, 4789–4792.
- [60] N. W. Gong, M. Y. Lu, C. Y. Wang, Y. Chen and L. J. Chen, Au(Si)-filled Beta-Ga₂O₃ nanotubes as wide range high temperature nanothermometers, *Appl. Phys. Lett.*, 2008,92, 073101–073103.
- [61] Y. B. Li, Y. Bando and D. Golberg, Single-crystalline In₂O₃ nanotubes filled with In, *Adv. Mater.*, 2003,15, 581–585.
- [62] P. D. Tovee, M. E. Pumarol, M. C. Rosamond, R. Jones, M. C. Petty, D. A. Zezeb and O. V. Kolosov, Nanoscale resolution scanning thermal microscopy using carbon nanotube tipped thermal probes, *Phys.Chem.Chem.Phys.*, 2014,16, 1174–1181.
- [63] P. R. N. Childs, *Practical Temperature Measurement*, Butterworth Heinemann, 2001.
- [64] J. Millen, T. Deesuwan, P. Barker and J. Anders, Nanoscale temperature measurements using non-equilibrium Brownian dynamics of a levitated nanosphere, *Nat. Nanotechnol.*, 2014.
- [65] Brites, C. D. S., Lima, P. P., Silva, N. J. O., Millán, A., Amaral, V. S., Palacio, F., Carlos, L. D. (2012). Thermometry at the nanoscale. *Nanoscale*, 4(16), 4799. <https://doi.org/10.1039/c2nr30663h>
- [66] T.H. Howard, *Diamond Synthesis* 2947608, 1955.

- [67] Nunn, N., Torelli, M., McGuire, G., Shenderova, O. (2017). Nanodiamond: A high impact nanomaterial. *Current Opinion in Solid State and Materials Science*, 21(1), 1–9. <https://doi.org/10.1016/j.cossms.2016.06.008>
- [68] D. Discher, C. Dong, J. Fredberg, F. Guilak, D. Ingber, P. Janmey, R. Kamm, G. Schmid-Schönbein, S. Weinbaum, *Biomechanics: cell research and applications for the next decade*, *Ann. Biomed. Eng.* 37 (5) (2009) 847–859.
- [69] T.L. Daulton, Extraterrestrial nanodiamonds in the cosmos, in: *Ultrananocrystalline Diamond*, William-Andrew, Norwich, UK, 2006, pp. 23– 79.
- [70] G.W. Yang, J.B. Wang, Q.X. Liu, Preparation of nano-crystalline diamonds using pulsed laser induced reactive quenching, *J. Phys. Condens. Mat.* 10 (1998).
- [71] J.-P. Boudou, P.A. Curmi, F. Jelezko, J. Wrachtrup, P. Aubert, M. Sennour, G. Balasubramanian, R. Reuter, A. Thorel, E. Gaffet, High yield fabrication of fluorescent nanodiamonds, *Nanotechnology* 20 (2009) 11.
- [72] M.W.D.J.K.E.R. Frenklach, W. Howard, D. Huang, J. Yuan, K. Spear, R. Koba, Induced nucleation of diamond powder, *Appl. Phys. Lett.* 59 (5) (1991) 546–548.
- [73] A. Kumar, P.A. Lin, A. Xue, B. Hao, Y.K. Yap, R.M. Sankaran, Formation of nanodiamonds at near-ambient conditions via microplasma dissociation of ethanol vapour, *Nat. Commun.* 5 (2013).
- [74] T.L. Daulton, M.A. Kirk, R.S. Lewis, L.E. Rehn, Production of nanodiamonds by high-energy ion irradiation of graphite at room temperature, *Nucl. Instrum. Meth. B* 175 (2001).
- [75] S. Welz, Y. Gogotsi, M.J. McNallan, Nucleation, growth, and graphitization of diamond nanocrystals during chlorination of carbides, *J. Appl. Phys.* 93 (2003).
- [76] F. Banhart, P.M. Ajayan, Carbon onions as nanoscopic pressure cells for diamond formation, *Nature* 382 (1996).
- [77] E. Galimov et al., Experimental corroboration of the synthesis of diamond in the cavitation process, *Dokl. Phys.* 49 (2004).
- [78] Mochalin, V.N., et al., The properties and applications of nanodiamonds. *Nature Nanotechnology*, 2012. 7(1): p. 11-23.

- [79] V.N. Mochalin, Y. Gogotsi, Nanodiamond–polymer composites, *Diamond Related Mater.* 58 (2015) 161–171; V.Y. Dolmatov, Detonation nanodiamonds: synthesis, structure, properties and applications, *Usp. Khim.* 76 (4) (2007) 376–397.
- [80] O. Shenderova, A. Vargas, S. Turner, D. Ivanov, M. Ivanov, Nanodiamond-based nanolubricants: investigation of friction surfaces, *Tribol. Trans.* 57 (6) (2014) 1051–1057.
- [81] O.A. Shenderoava, V. Grichko, Nanodiamond UV Protectant Formulations, US Patent 8753614, 2005; UV Protective Coatings, US Patent 9296656, 2005.
- [82] S.J. Yu, M.-W. Kang, H.C. Chang, K.-M. Chen, Y.C. Yu, Bright fluorescent nanodiamonds: no photobleaching and low cytotoxicity, *J. Am. Chem. Soc.* 127 (50) (2005) 17604–17605.
- [83] Ferrari, A.C. and J. Robertson, Interpretation of Raman spectra of disordered and amorphous carbon. *Physical Review B*, 2000. 61(20): p. 14095-14107.
- [84] O. Shenderova, I. Vlasov, S.A.C. Hens, V. Borjanovic, Enhancement of Photoluminescence of Nanodiamond Particles. US Patent 9260653, 2010.
- [85] R. Schirhagl, K. Chang, M. Loretz, C.L. Degen, Nitrogen-vacancy centers in diamond: nanoscale sensors for physics and biology, *Ann. Rev. Phys. Chem.* 65 (2014).
- [86] M.W. Doherty, N.B. Manson, P. Delaney, F. Jelezko, J. Wrachtrup, L.C. Hollenberg, The nitrogen-vacancy colour centre in diamond, *Phys. Rep.* 528 (1) (2013) 1–45.
- [87] V. Vijayanthimala, D.K. Lee, S.V. Kim, A. Yen, N. Tsai, D. Ho, H. C. Chang, O. Shenderova, Nanodiamond-mediated drug delivery and imaging: challenges and opportunities, *Exp. Opin. Drug Deliv.* 12 (5) (2015) 735–749.
- [88] E.K.-H. Chow, D. Ho, Cancer nanomedicine: from drug delivery to imaging, *Sci. Transl. Med.* 5 (216) (2013) 216rv4.
- [89] E.K. Chow, X.Q. Zhang, M. Chen, R. Lam, E. Robinson, H. Huang, D. Schaffer, E. Osawa, A. Goga, D. Ho, Nanodiamond therapeutic delivery agents mediate enhanced chemoresistant tumor treatment, *Sci. Transl. Med.* 3 (73) (2011).
- [90] Ager III, J.W., D.K. Veirs, and G.M. Rosenblatt, Spatially resolved Raman studies of diamond films grown by chemical vapor deposition. *Physical Review B*, 1991. 43(8): p. 6491

- [91] Sapsford, K.E., et al., Functionalizing Nanoparticles with Biological Molecules: Developing Chemistries that Facilitate Nanotechnology. *Chemical Reviews*, 2013. 113(3): p. 1904-2074.
- [92] Petit, T., et al., Probing Interfacial Water on Nanodiamonds in Colloidal Dispersion. *Journal of Physical Chemistry Letters*, 2015. 6(15): p. 2909-2912.
- [93] Santacruz-Gomez, K., Silva-Campa, E., Melendrez-Amavizca, R., Teran Arce, F., Mata-Haro, V., Landon, P. B., Lal, R. (2016). Carboxylated nanodiamonds inhibit γ -irradiation damage of human red blood cells. *Nanoscale*, 8(13), 7189–7196. <https://doi.org/10.1039/C5NR06789H>
- [94] Rendler, T. (2018). Fluorescent nanodiamonds as a sensor and life science probe.
- [95] Kamatchi Jothiramalingam Sankaran, Yen-Fu Lin, Wen-Bin Jian, Huang-Chin Chen, Kalpataru Panda, Balakrishnan Sundaravel, Chung-Li Dong, Nyan-Hwa Tai, and I-Nan Lin, Structural and electrical properties of conducting diamond nanowires, *ACS Applied Materials Interfaces* 5 (2013), no. 4, 1294–1301, PMID: 23327783.
- [96] <http://www.bris.ac.uk/depts/chemistry/motm/diamond/diamond.htm>
- [97] Reza Abbaschian, Henry Zhu, and Carter Clarke, High pressure–high temperature growth of diamond crystals using split sphere apparatus, *Diamond and Related Materials* 14 (2005), no. 11, 1916–1919.
- [98] Yu Borzdov, Yu Pal'yanov, I Kupriyanov, V Gusev, A Khokhryakov, A Sokol, and A Efremov, HPHT synthesis of diamond with high nitrogen content from an Fe₃N-C system, *Diamond and Related Materials* 11 (2002), no. 11, 1863–1870.
- [99] Yafei Zhang, Chuanyi Zang, Hongan Ma, Zhongzhu Liang, Lin Zhou, Shangsheng Li, and Xiaopeng Jia, HPHT synthesis of large single crystal diamond doped with high nitrogen concentration, *Diamond and Related Materials* 17 (2008), no. 2, 209–211.
- [100] Stepan Stehlik, Marian Varga, Martin Ledinsky, Vit Jirasek, Anna Artemenko, Halyna Kozak, Lukas Ondic, Viera Skakalova, Giacomo Argentero, Timothy Pennycook, Jannik C Meyer, Antonin Fejfar, Alexander Kromka, and Bohuslav Rezek, Size and Purity Control of HPHT Nanodiamonds down to 1 nm, *Journal of Physical Chemistry C* 119 (2015), no. 49, 27708–27720.

- [101] K.L. Choy, Chemical vapour deposition of coatings, *Progress in Materials Science* 48 (2003), no. 2, 57–170.
- [102] V. F. Tatsii, A. V. Bochko, and G. S. Oleinik, Structure and Properties of Detonation Diamonds, *Combustion, Explosion, and Shock Wave* 45 (2009), no. 1, 95–103.
- [103] William A. Goddard III, Donald W. Brenner, Sergey Edward Lyshevski, and Gerald J. Iafrate, *Handbook of nanoscience, engineering, and technology*, CRC Press, 2012.
- [104] Olga A. Shenderova, Igor I. Vlasov, Stuart Turner, Gustaaf Van Tendeloo, Sergey B. Orlinskii, Andrey A. Shiryaev, Andrey A. Khomich, Sergey N. Sulyanov, Fedor Jelezko, and Joerg Wrachtrup, Nitrogen Control in Nanodiamond Produced by Detonation Shock-Wave-Assisted Synthesis, *The Journal of Physical Chemistry C* 115 (2011), no. 29, 14014–14024.
- [105] A. S. Barnard and M. Sternberg, Substitutional nitrogen in nanodiamond and bucky-diamond particles, *Journal of Physical Chemistry B* 109 (2005), no. 36, 17107–17112.
- [106] Dimitar P. Mitev, Ashley T. Townsend, Brett Paull, and Pavel N. Nesterenko, Microwave-assisted purification of detonation nanodiamond, *Diamond and Related Materials* 48 (2014), 37–46.
- [107] Stepan Stehlik, Marian Varga, Martin Ledinsky, Daria Miliarieva, Halyna Kozak, Viera Skakalova, Clemens Mangler, Timothy J. Pennycook, Jannik C. Meyer, Alexander Kromka, and Bohuslav Rezek, High-yield fabrication and properties of 1.4 nm nanodiamonds with narrow size distribution, *Scientific Reports* 6 (2016), 38419.
- [108] Alexandr M. Zaitsev, *Optical Properties of Diamond : a Data Handbook*, Springer-Verlag, 2001.
- [109] E. van Oort, N. B. Manson, and M. Glasbeek, Optically detected spin coherence of the diamond n-v centre in its triplet ground state, *Journal of Physics, Solid State Physics* 21 (1988), no. 23, 4385.
- [110] Schirhagl, R., Chang, K., Loretz, M., Degen, C. L. (2014). Nitrogen-Vacancy Centers in Diamond: Nanoscale Sensors for Physics and Biology. *Annual Review of Physical Chemistry*, 65(1), 83–105. <https://doi.org/10.1146/annurev-physchem-040513-103659>
- [111] Doherty, M. W., Manson, N. B., Delaney, P., Jelezko, F., Wrachtrup, J., Hollenberg, L. C. L. (2013). The nitrogen-vacancy colour centre in diamond. *Physics Reports*, 528(1), 1–45. <https://doi.org/10.1016/j.physrep.2013.02.001>

- [112] Florian Dolde, Helmut Fedder, Marcus W. Doherty, Tobias Nöbauer, Florian Rempp, Gopalakrishnan Balasubramanian, Thomas Wolf, Friedemann Reinhard, Lloyd C. L. Hollenberg, Fedor Jelezko, and Jörg Wrachtrup, Sensing electric fields using single diamond spins, *Nature Physics* 7 (2011), 459–463.
- [113] Kasper Jensen, Pauli Kehayias, and Dmitry Budker, *Magnetometry with nitrogen-vacancy centers in diamond*, pp. 553–576, Springer International Publishing, Cham, 2017.
- [114] P. Neumann, I. Jakobi, F. Dolde, C. Burk, R. Reuter, G. Waldherr, J. Honert, T. Wolf, A. Brunner, J. H. Shim, D. Suter, H. Sumiya, J. Isoya, and J. Wrachtrup, High-Precision Nanoscale Temperature Sensing Using Single Defects in Diamond, *Nano Letters* 13 (2013), no. 6, 2738–2742.
- [115] David M. Toyli, Charles F. de las Casas, David J. Christle, Viatcheslav V. Dobrovitski, and David D. Awschalom, Fluorescence thermometry enhanced by the quantum coherence of single spins in diamond, *Proceedings of the National Academy of Sciences of the United States of America* 110 (2013), no. 21, 8417–8421.
- [116] T. Staudacher, F. Shi, S. Pezzagna, J. Meijer, J. Du, C. A. Meriles, F. Reinhard, and J. Wrachtrup, Nuclear Magnetic Resonance Spectroscopy on a (5-Nanometer)³ Sample Volume, *Science* 339 (2013), no. 6119, 561–563.
- [117] Abdelghani Laraoui, Florian Dolde, Christian Burk, Friedemann Reinhard, Jörg Wrachtrup, and Carlos A. Meriles, High-resolution correlation spectroscopy of ¹³C spins near a nitrogen-vacancy centre in diamond, *Nature Communications* 4 (2013), 1651.
- [118] Nabeel Aslam, Matthias Pfender, Philipp Neumann, Rolf Reuter, Andrea Zappe, Felipe Fávoro de Oliveira, Andrej Denisenko, Hitoshi Sumiya, Shinobu Onoda, Junichi Isoya, and Jörg Wrachtrup, Nanoscale nuclear magnetic resonance with chemical resolution, *Science* 357 (2017), 67–71.
- [119] Xing Rong, Jianpei Geng, Fazhan Shi, Ying Liu, Kebiao Xu, Wenchao Ma, Fei Kong, Zhen Jiang, Yang Wu, and Jiangfeng Du, Experimental fault-tolerant universal quantum gates with solid-state spins under ambient conditions, *Nature Communications* 6 (2015), 8748.

-
- [120] J. R. Maze, A. Gali, E. Togan, Y. Chu, A. Trifonov, E. Kaxiras, and M. D. Lukin, Properties of nitrogen-vacancy centers in diamond: the group theoretic approach, *New Journal of Physics* 13 (2011), no. 2, 025025.
- [121] M. W. Doherty, N. B. Manson, P. Delaney, and L. C. L. Hollenberg, The negatively charged nitrogen-vacancy centre in diamond: the electronic solution, *New Journal of Physics* 13 (2011), no. 2, 025019.
- [122] L. J. Rogers, S. Armstrong, M. J. Sellars, and Manson, Infrared emission of the NV centre in diamond: Zeeman and uniaxial stress studies, *New Journal of Physics* 10 (2008), no. 10, 103024.
- [123] J. Harrison, M. J. Sellars, and N. B. Manson, Optical spin polarisation of the N-V centre in diamond, *Journal of Luminescence* 107 (2004), no. 1, 245–248.
- [124] Adam Gali, Theory of the neutral nitrogen-vacancy center in diamond and its application to the realization of a qubit, *Physical Review B* 79 (2009), no. 23, 235210.
- [125] Bernhard Grotz, Moritz V. Hauf, Markus Dankerl, Boris Naydenov, Sébastien Pezzagna, Jan Meijer, Fedor Jelezko, Jörg Wrachtrup, Martin Stutzmann, Friedemann Reinhard, and Jose A. Garrido, Charge state manipulation of qubits in diamond, *Nature communications* 3 (2012), 729.
- [126] M. V. Hauf, B. Grotz, B. Naydenov, M. Dankerl, S. Pezzagna, J. Meijer, F. Jelezko, J. Wrachtrup, M. Stutzmann, F. Reinhard, and J. A. Garrido, Chemical control of the charge state of nitrogen-vacancy centers in diamond, *Physical Review B* 83 (2011), no. 8, 081304(R).
- [127] Matthias Pfender, Nabeel Aslam, Patrick Simon, Denis Antonov, Gergő Thiering, Sina Burk, Felipe Fávoro de Oliveira, Andrej Denisenko, Helmut Fedder, Jan Meijer, Jose A. Garrido, Adam Gali, Tokuyuki Teraji, Junichi Isoya, Marcus William Doherty, Audrius Alkauskas, Alejandro Gallo, Andreas Grüneis, Philipp Neumann, and Jörg Wrachtrup, Protecting a Diamond Quantum Memory by Charge State Control, *Nano Letters* 17 (2017), no. 10, 5931–5937.
- [128] Nabeel Aslam, Gerhald Waldherr, Philipp Neumann, Fedor Jelezko, and Joerg Wrachtrup, Photo-induced ionization dynamics of the nitrogen vacancy defect in diamond investigated by single-shot charge state detection, *New Journal of Physics* 15 (2013), no. 1, 013064.

- [129] P. Siyushev, H. Pinto, M. Vörös, A. Gali, F. Jelezko, and J. Wrachtrup, Optically Controlled Switching of the Charge State of a Single Nitrogen- Vacancy Center in Diamond at Cryogenic Temperatures, *Physical Review Letters* 110 (2013), no. 16, 167402.
- [130] Lucio Robledo, Hannes Bernien, Ilse Van Weperen, and Ronald Hanson, Control and Coherence of the Optical Transition of Single Nitrogen Vacancy Centers in Diamond, *Physical Review Letters* 105 (2010), no. 17, 177403.
- [131] Siddharth Dhomkar, Jacob Henshaw, Harishankar Jayakumar, and Carlos A. Meriles, Long-term data storage in diamond, *Science Advances* 2 (2016), no. 10, e1600911.
- [132] T. Gaebel, M. Domhan, C. Wittmann, I. Popa, F. Jelezko, J. Rabeau, A. Greentree, S. Praver, E. Trajtkov, P.R. R. Hemmer, and J. Wrachtrup, Photochromism in single nitrogen-vacancy defect in diamond, *Applied Physics B: Lasers and Optics* 82 (2006), no. 2, 243–246.
- [133] N.B. Manson and J.P. Harrison, Photo-ionization of the nitrogen-vacancy center in diamond, *Diamond and Related Materials* 14 (2005), no. 10, 1705– 1710.
- [134] Moloud Kaviani, Peter Deák, Bálint Aradi, Thomas Frauenheim, Jyh Pin Chou, and Adam Gali, Proper surface termination for luminescent near- surface NV centers in diamond, *Nano Letters* 14 (2014), no. 8, 4772–4777.
- [135] L. Rondin, G. Dantelle, a. Slablab, F. Grosshans, F. Treussart, P. Bergonzo, S. Peruchas, T. Gacoin, M. Chaigneau, H.-C. Chang, V. Jacques, and J.-F. Roch, Surface-induced charge state conversion of nitrogen-vacancy defects in nanodiamonds, *Physical Review B* 82 (2010), no. 11, 115449.
- [136] K.-M. C. Fu, C. Santori, P. E. Barclay, and R. G. Beausoleil, Conversion of neutral nitrogen-vacancy centers to negatively charged nitrogen-vacancy centers through selective oxidation, *Applied Physics Letters* 96 (2010), no. 12, 121907.
- [137] C Bradac, T Gaebel, N Naidoo, M J Sellars, J Twamley, L J Brown, A S Barnard, T Plakhotnik, A V Zvyagin, and J R Rabeau, Observation and control of blinking nitrogen-vacancy centres in discrete nanodiamonds, *Nature Nanotechnology* 5 (2010), no. 5, 345–349.

- [138] F. Dolde, I. Jakobi, B. Naydenov, N. Zhao, S. Pezzagna, C. Trautmann, J. Meijer, P. Neumann, F. Jelezko, and J. Wrachtrup, Room-temperature entanglement between single defect spins in diamond, *Nature Physics* 9 (2013), 139–143.
- [139] P. Spinicelli, A. Dréau, L. Rondin, F. Silva, J. Achard, S. Xavier, S. Bansropun, T. Debuisschert, S. Pezzagna, J. Meijer, V. Jacques, and J-F Roch, Engineered arrays of nitrogen-vacancy color centers in diamond based on implantation of CN molecules through nanoapertures, *New Journal of Physics* 13 (2011), no. 2, 025014.
- [140] David M. Toyli, Christoph D. Weis, Gregory D. Fuchs, Thomas Schenkel, and David D. Awschalom, Chip-scale nanofabrication of single spins and spin arrays in diamond, *Nano letters* 10 (2010), no. 8, 3168–3172.
- [141] B. Naydenov, S. Pezzagna, F. Dolde, F. Jelezko, J. Wrachtrup, C. Trautmann, and J. Meijer, Nano-pore channels in a mica sheet with high aspect ratio as a mask, *GSI SCIENTIFIC REPORT* (2010), 2010.
- [142] Sébastien Pezzagna, Dominik Wildanger, Paul Mazarov, Andreas D. Wieck, Yanko Sarov, Ivo Rangelow, Boris Naydenov, Fedor Jelezko, Stefan W. Hell, and Jan Meijer, Nanoscale Engineering and Optical Addressing of Single Spins in Diamond, *Small* 6 (2010), no. 19, 2117–2121.
- [143] Wolfgang Schnitzler, Georg Jacob, Robert Fickler, Ferdinand Schmidt-Kaler, and Kilian Singer, Focusing a deterministic single-ion beam, *New Journal of Physics* 12 (2010), no. 6, 065023.
- [144] Michael I. Current, Norman L. Turner, T.C. Smith, and Dave Crane, Planar channeling effects in Si(100), *Nuclear Instruments and Methods in Physics Research Section B: Beam Interactions with Materials and Atoms* 6 (1985), 336–348.
- [145] Boris Naydenov, V. Richter, Johannes Beck, Matthias Steiner, Philipp Neumann, Gopalakrishnan Balasubramanian, Jocelyn Achard, Fedor Jelezko, Joerg Wrachtrup, and Rafi Kalish, Enhanced generation of single optically active spins in diamond by ion implantation, *Applied Physics Letters* 96 (2010), no. 16, 163108.
- [146] Felipe Fávoro de Oliveira, Seyed Ali Momenzadeh, Denis Antonov, Helmut Fedder, Andrej Denisenko, and Jörg Wrachtrup, On the efficiency of combined ion implantation for the creation of near-surface nitrogen-vacancy centers in diamond, *Physica Status Solidi (A) Applications and Materials Science* 213 (2016), no. 8, 2044–2050.

- [147] Boris Naydenov, V. Richter, Johannes Beck, Matthias Steiner, Philipp Neumann, Gopalakrishnan Balasubramanian, Jocelyn Achard, Fedor Jelezko, Joerg Wrachtrup, and Rafi Kalish, Enhanced generation of single optically active spins in diamond by ion implantation, *Applied Physics Letters* 96 (2010), no. 16, 163108.
- [148] Felipe Fávoro de Oliveira, Seyed Ali Momenzadeh, Denis Antonov, Helmut Fedder, Andrej Denisenko, and Jörg Wrachtrup, On the efficiency of combined ion implantation for the creation of near-surface nitrogen-vacancy centers in diamond, *Physica Status Solidi (A) Applications and Materials Science* 213 (2016), no. 8, 2044–2050.
- [149] Felipe Fávoro De Oliveira, Denis Antonov, Ya Wang, Philipp Neumann, Seyed Ali Momenzadeh, Timo Häuermann, Alberto Pasquarelli, Andrej Denisenko, and Jörg Wrachtrup, Tailoring spin defects in diamond by lattice charging, *Nature Communications* 8 (2017), 15409.
- [150] Kenichi Ohno, F. Joseph Heremans, Lee C. Bassett, Bryan A. Myers, David M. Toyli, Ania C. Bleszynski Jayich, Christopher J. Palmstrøm, and David D. Awschalom, Engineering shallow spins in diamond with nitrogen delta-doping, *Applied Physics Letters* 101 (2012), no. 8, 082413.
- [151] Julia Michl, Tokuyuki Teraji, Sebastian Zaiser, Ingmar Jakobi, Gerald Waldherr, Florian Dolde, Philipp Neumann, Marcus W. Doherty, Neil B. Manson, Junichi Isoya, and Jörg Wrachtrup, Perfect alignment and preferential orientation of nitrogen-vacancy centers during chemical vapor deposition diamond growth on (111) surfaces, *Applied Physikal Letters* 104 (2014), no. 10, 102407.
- [152] Jan Havlik, Vladimira Petrakova, Ivan Rehor, Vaclav Petrak, Michal Gulka, Jan Stursa, Jan Kucka, Jan Ralis, Torsten Rendler, San-Yung Lee, Rolf Reuter, Joerg Wrachtrup, Miroslav Ledvina, Milos Nesladek, and Petr Cigler, Boosting nanodiamond fluorescence: towards development of brighter probes, *Nanoscale* 5 (2013), no. 8, 3208.
- [153] A. G. Alekseev, V. N. Amosov, a. V. Krasil'nikov, S. N. Tugarinov, V. V. Frunze, and a. Yu. Tsutskikh, Transformation of GR1 defects in annealed natural type IIa diamonds, *Technical Physics Letters* 26 (2000), no. 6, 496–498.
- [154] Xuerui Song, Guanzhong Wang, Xiaodi Liu, Fupan Feng, Junfeng Wang, Liren Lou, and Wei Zhu, Generation of nitrogen-vacancy color center in nanodiamonds by high temperature annealing, *Applied Physics Letters* 102 (2013), no. 13, 133109.

- [155] Boris Naydenov, Friedemann Reinhard, Anke Laemmle, V. Richter, Rafi Kalish, Ulrika F. S. D’Haenens-Johansson, Mark Newton, Fedor Jelezko, and Joerg Wrachtrup, Increasing the coherence time of single electron spins in diamond by high temperature annealing, *Applied Physics Letters* 97 (2010), no. 24, 242511.
- [156] A. S. Barnard, S P Russo, and I K Snook, Size dependent phase stability of carbon nanoparticles: Nanodiamond versus fullerenes, *The Journal of Chemical Physics* 118 (2003), no. 11, 5094.
- [157] Carlo Bradac, Torsten Gaebel, Nishen Naidoo, James R. Rabeau, and Amanda S. Barnard, Prediction and Measurement of the Size-Dependent Stability of Fluorescence in Diamond over the Entire Nanoscale, *Nano Letters* 9 (2009), no. 10, 3555–3564. 17107–17112.
- [158] Igor I. Vlasov, Amanda S. Barnard, Victor G. Ralchenko, Oleg I. Lebedev, Mikhail V. Kanzyuba, Alexey V. Saveliev, Vitaly I. Konov, and Etienne Goovaerts, Nanodiamond Photoemitters Based on Strong Narrow-Band Luminescence from Silicon-Vacancy Defects, *Advanced Materials* 21 (2009), no. 7, 808–812.
- [159] A. S. Barnard, I. I. Vlasov, and V. G. Ralchenko, Predicting the distribution and stability of photoactive defect centers in nanodiamond biomarkers, *Journal of Materials Chemistry* 19 (2009), no. 3, 360.
- [160] Chenguang Wang, Masayasu Taki, Yoshikatsu Sato, Aiko Fukazawa, Tetsuya Higashiyama, and Shigehiro Yamaguchi, Super-Photostable Phosphole-Based Dye for Multiple-Acquisition Stimulated Emission Depletion Imaging, *Journal of the American Chemical Society* 139 (2017), no. 30, 10374–10381.
- [161] C Bradac, T Gaebel, N Naidoo, M J Sellars, J Twamley, L J Brown, A S Barnard, T Plakhotnik, A V Zvyagin, and J R Rabeau, Observation and control of blinking nitrogen-vacancy centres in discrete nanodiamonds, *Nature Nanotechnology* 5 (2010), no. 5, 345–349.
- [162] Asaf Bolker, Cecile Saguy, Moshe Tordjman, and Rafi Kalish, Quantum confinement and Coulomb blockade in isolated nanodiamond crystallites, *Physical Review B* 88 (2013), no. 3, 035442.
- [163] Jean-Yves Raty, Giulia Galli, C. Bostedt, Tony W. Van Buuren, and Louis J. Terminello, Quantum Confinement and Fullerene-like Surface Reconstructions in Nanodiamonds, *Physical Review Letters* 90 (2003), no. 3, 037401.

- [164] Kehayias, P. M. (2015). Exploring Basic Properties and Applications of Nitrogen-Vacancy Color Centers in Diamond. PhD Thesis.
- [165] <https://www.ugr.es/~decacien/Planes/Quimica/Plan%201997/temarios/671111d-archivos/fundamentos/SEMINARIO%203.PDF>
- [166] <https://www.chem.uci.edu/~dmitryf/manuals/Fundamentals/Fluorescence%20Spectroscopy.pdf>
- [167] Pedroso-santana, S., Sarabia-saínz, A., Fleitas-salazar, N., Santacruz-gómez, K., Acosta-elías, M., Pedroza-montero, M., Riera, R. (2017). Deagglomeration and characterization of detonation nanodiamonds for biomedical applications, 15, 15–21.
- [168] Plakhotnik, T., Aman, H., Chang, H.C. (2015). All-optical single-nanoparticle ratio-metric thermometry with a noise floor of $0.3 \text{ K Hz}^{1/2}$. *Nanotechnology*, 26(24), 245501. <https://doi.org/10.1088/0957-4484/26/24/245501>